Journal of Rock Mechanics and Geotechnical Engineering 18 (2026) 3539–3554

Contents lists available at ScienceDirect

Journal of Rock Mechanics and Geotechnical Engineering

journal homepage: www.jrmge.cn

Full Length Article

Improved phase field simulation of 3D multiple cracks propagation in rock materials via unified shear energy criterion

Susheng Wang [a,b,c], Sheng-Qi Yang [a], Qiang Zhang [c,*], Changdong Ding [d], Qingfu Huang [e], Wanqing Shen [f]

[a] State Key Laboratory of Intelligent Deep Metal Mining and Equipment, Shaoxing University, Shaoxing, 312000, China
[b] Zhejiang Key Laboratory of Rock Mechanics and Geohazards, School of Civil Engineering, Shaoxing University, Shaoxing, 312000, China
[c] State Key Laboratory of Water Cycle and Water Security, China Institute of Water Resources and Hydropower Research, Beijing, 100038, China
[d] Key Laboratory of Geotechnical Mechanics and Engineering of Ministry of Water Resources, Changjiang River Scientific Research Institute, Wuhan, 430010, China
[e] PowerChina Kunming Engineering Corporation Limited, Kunming, 650051, China
[f] Laboratory of Multiscale and Multiphysics Mechanics, University of Lille, CNRS FRE 2016, LaMcube, Lille, 59000, France

ARTICLE INFO

Article history:
Received 14 January 2025
Received in revised form
26 July 2025
Accepted 17 August 2025
Available online 15 December 2025

Keywords:
Phase-field method (PFM)
Rock materials
Compressive-shear cracks
Triple shear energy strength (TSES) criterion
3D multiple cracks propagation

ABSTRACT

The phase-field method (PFM) has emerged as a robust tool for fracture simulation; however, applying this technique to rock materials poses significant challenges, particularly in accurately modeling the propagation of multiple cracks in the presence of complex three-dimensional (3D) mixed-mode loading involving tensile, tensile-shear, and compressive-shear cracks. To address these limitations, this study aims to introduce an enhanced PFM that integrates frictional effects and Lode angle dependence while unifying the volumetric deviatoric (VD) and spectral decomposition (SD) methods. The proposed model incorporates a modified driving force for 3D compressive-shear cracks by embedding a triple shear energy strength (TSES) criterion within the energy decomposition framework. This refinement guarantees that crack behavior remains physically realistic under compression-dominated loading while effectively preserving well-established tensile fracture mechanisms. The validation of the numerical implementation is also conducted through both analytical verification against theoretical solutions and 3D finite element simulations of fissured rock and heterogeneous specimens. Furthermore, numerical case studies demonstrate the model's ability to effectively capture the 3D propagation of multiple cracks and replicate realistic true 3D mechanical responses. The findings present valuable insights and practical guidelines for the application of PFM in rock engineering.

1. Introduction

In the fields of hydropower development, mining, and radioactive waste disposal engineering, rocks are often employed as host materials in underground engineering projects. As excavation and construction activities advance into deeper and more complex geological environments, the stress induced by excavation could lead to a three-dimensional (3D) stress redistribution and the formation of what is known as an excavation damaged zone (EDZ) (Perras and Diederichs, 2016). The primary mechanism responsible for the formation of ultimate macroscopic damage is mainly linked to the propagation and collapse of multiple cracks (Zhang et al., 2024). As a result, persistent damage and deterioration of the surrounding rock could lead to significant engineering disasters, such as slabbing failures (Du et al., 2016), rockbursts (Ortlepp and Stacey, 1994), fault slips (Bhattacharya and Viesca, 2019), and structural collapses (Xiao et al., 2016). Furthermore, the prevailing stress state plays a critical role in the behavior of the EDZ (Eberhardt, 2001; Diederichs et al., 2004; Li et al., 2024; Wang et al., 2025a, 2025b), which subsequently influences the selection of the tunnel axis in underground engineering projects. Therefore, accurately predicting the propagation of 3D multiple cracks under polyaxial stress conditions presents a formidable challenge that is essential for conducting stability analyses and mitigating potential geological disasters.

* Corresponding author.
E-mail address: zhangq@iwhr.com (Q. Zhang).

Peer review under responsibility of Institute of Rock and Soil Mechanics, Chinese Academy of Sciences.

https://doi.org/10.1016/j.jrmge.2025.08.045

The phase-field method (PFM) is a robust and nonlocal technique adept at addressing discontinuous problems in solids. It is developed from the Griffith theory through a regularization energy-based numerical approach with variational formulations. The complexities associated with the propagation of multiple cracks can be reformulated as a multi-field problem during the computational process. A significant advantage of this method is its automatic tracking of the cracking process, thereby eliminating the need for additional tracking algorithms and ad-hoc criteria (Zhang et al., 2017b; Piska et al., 2024). This approach also effectively replicates intricate crack patterns, encompassing nucleation, propagation, bifurcation, and merging. Moreover, it partially alleviates the issue of grid dependence (Nguyen et al., 2016) often encountered in traditional continuum damage models by employing nonlocal regularization through the gradient formulation of the phase field (Singh et al., 2016), which incorporates the interdependence between neighboring elements. Over the past two decades, this approach has gained considerable attention and has been extensively researched. Initially applied to brittle fracture, the phase-field approach has since been adopted to tackle a diverse array of fracture related challenges, mainly including 3D phase-field applications (Wu et al., 2021; Zhuang et al., 2023; Hai et al., 2024a, 2024b), ductile fracture with large deformation (You et al., 2020), hydro-mechanical coupling fracture (Yu et al., 2021b), dynamic fracture (Tian et al., 2019), heat-induced cracking (Zhao et al., 2023), and multi-physics field coupling issues (Yu et al., 2021a).

In conventional PFM for fracture, crack propagation is primarily driven by the tensile component of strain energy utilizing either the volumetric deviatoric (VD) method (Amor et al., 2009) or the spectral decomposition (SD) method (Miehe et al., 2010a). These approaches effectively address tension-compression asymmetry by focusing exclusively on tensile contributions to the fracture driving energy, thus preventing non-physical crack propagation under compression conditions. Nonetheless, rock materials exhibit particularly intricate fracture behavior due to the unilateral effects and mixed-mode fracture mechanisms that arise under complex loading scenarios (Zhu et al., 2011). While these decomposition methods excel in preventing damage during pure hydrostatic compression ($\sigma_1 = \sigma_2 = \sigma_3$) (Wong and Baud, 2012), they may not adequately capture compressive-shear dominated fracture phenomena that can manifest under specific stress states, especially when frictional effects are significant.

PFM has undergone significant development for two-dimensional (2D) scenarios under plane strain/stress assumptions (Fei and Choo, 2021; Li et al., 2021; Feng and Li, 2023). However, substantial challenges persist in modeling 3D fracture phenomena in rock materials. Current methodologies frequently struggle to precisely predict the interactions between multiple cracks and the combined influences of stress conditions and friction factors on compressive-shear fractures. These limitations become especially evident when translating qualitative fracture patterns into quantitative engineering design criteria. To address these pressing challenges, our research advances the conventional framework through two key innovations: (1) the incorporation of frictional dissipation mechanisms for 3D compressive-shear cracks, and (2) the innovative unification of the established VD and SD approaches. This hybrid methodology facilitates physically realistic simulations of 3D fracture networks within rock masses while maintaining the well-validated predictive capabilities for tensile fracture behavior.

This paper presents an enhanced PFM for modeling 3D crack propagation in rock materials. The subsequent sections are organized as follows. Section 2 establishes the validity of the three-shear strength criterion by evaluating experimental 3D results of conventional triaxial compression (CTC) and true triaxial compression (TTC) tests on typical quasi-brittle rocks. The results demonstrate its robustness as a broadly applicable criterion for characterizing material strength. In Section 3, a modified PFM is developed by incorporating a novel compressive-shear strain energy formulation. Section 4 details the finite element implementation of the proposed PFM and provides benchmark validations. Section 5 presents several representative numerical examples to illustrate the capability of the enhanced PFM in simulating complex 3D multiple crack propagation. The main conclusions and suggestions are summarized in the conclusions section. Additionally, Appendix A derives the theoretical framework of the triple shear energy strength (TSES) criterion based on shear strain energy, while Appendix B elaborates on the finite element discretization and implementation specifics of the PFM.

2. Validation of TSES criterion

Strength criteria define the stress, strain, or energy conditions under which materials reach their ultimate strength or failure state. In geotechnical engineering, where compressive-shear failure dominates, the TSES criterion offers distinct advantages by capturing the complete 3D failure mechanisms of rock materials through an energy-based approach. This section aims to validate the efficacy of the TSES criterion in predicting rock failure.

The TSES criterion is particularly well-suited for geotechnical applications, as it explicitly incorporates the frictional characteristics and compressive-shear failure mechanisms inherent in rock materials. Based on previous works (Gao et al., 2007; Li et al., 2020), the criterion posits that failure occurs when the cumulative shear strain energy on three orthogonal planes reaches a critical threshold as defined in Eq. (1).

$$f_p = p\sin\varphi + \frac{q}{\sqrt{3}}\cos\theta - \frac{q}{3}\sin\theta\sin\varphi - \eta \tag{1}$$

where φ represents the frictional angle; θ denotes the Lode angle; p is the mean stress, defined as $p = \sigma_{kk}/3$; q is the deviatoric stress, defined as $q = \sqrt{3J_2}$; and J_2 is the second invariant of the stress tensor. The parameter η ensures that compatibility with the Mohr-Coulomb (MC) criterion under CTC condition ($\sigma_2 = \sigma_3$) is satisfied, thereby preserving the physical interpretability. Unlike conventional stress-based criteria, this energy-based formulation naturally accounts for 3D compressive-shear interactions, addressing key limitations in existing models. A full theoretical derivation is provided in Appendix A.

The universality of the aforementioned strength theory requires rigorous validation using experimental data from typical quasi-brittle rocks. The CTC and TTC tests serve as effective laboratory methods for characterizing the mechanical behavior of rocks. Due to their simplicity and cost-effectiveness, CTC tests have been widely conducted, yielding abundant data. In this study, we evaluate the strength criterion using experimental data from five quasi-brittle rocks: sandstone (Yang et al., 2022), Kuru granite (Tkalich et al., 2016), dacite (Wang et al., 2019), basalt (Cai et al., 2021), and Beishan granite (Chen et al., 2015). The validity of the criterion is assessed by comparing the predicted peak strength with the test results, as illustrated in Fig. 1. The high correlation coefficients ($R^2 > 0.98$) for all datasets confirm that the criterion accurately captures the experimental strength relationship.

Since rock masses in engineering applications are subjected to true 3D stress states, the strength criterion is further validated using TTC test data. While CTC tests have historically been employed due to experimental limitations, advancements in TTC testing equipment have enabled more comprehensive

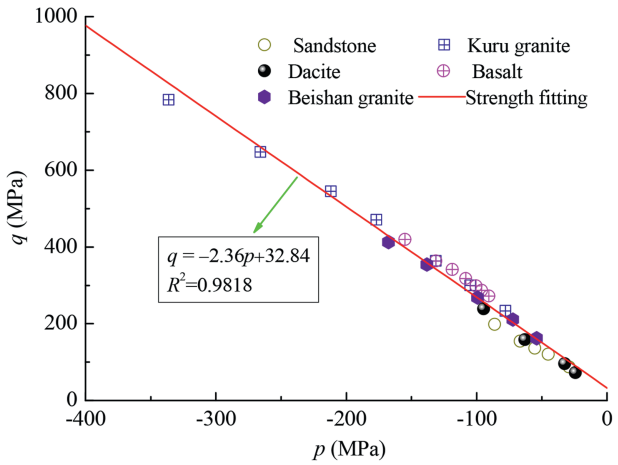

Fig. 1. Strength envelope fitting versus experimental results for five quasi-brittle rocks in CTC tests.

investigations. Ma and Haimson (2016) conducted systematic TTC tests on two porous sandstones: Bentheim (porosity ≈ 24%) and Coconino (porosity ≈ 17.5%), examining the effects of the intermediate principal stress (σ_2), failure modes, and micromorphology across a broad stress range. This range included CTC ($\sigma_1 = \sigma_2 \geq \sigma_3$) and generalized triaxial extension ($\sigma_1 \geq \sigma_2 = \sigma_3$), where tension is treated as positive. Notably, compaction bands observed in high-porosity Bentheim sandstone, associated with pore collapse and grain crushing under high confining pressure, fall beyond the scope of this study. Instead, Coconino sandstone was selected as a representative case for analyzing compressive-shear failure. The test results (Fig. 2) demonstrate that compressive-shear failure dominates under true 3D stress conditions. Here, σ_i^* (i = 1, 2, 3) denotes the stress values reported in the original study.

Fig. 3 shows the capability of the proposed criterion to describe the experimental strengths under varying σ_2^* and σ_3^*. The TSES criterion effectively captures the trend of peak strength variation with respect to σ_2^*, though minor discrepancies arise due to the assumption of constant friction angle and cohesion. The previous study (Feng et al., 2020) suggested that σ_2^* may influence frictional behavior, which could explain these deviations. In summary, the TSES criterion, derived from energy considerations and incorporating elastic parameters, strength parameters, and the Lode angle, extends the classical MC and Von-Mises criteria. Its applicability to quasi-brittle rocks is well-supported by experimental evidence.

3. A modified PFM

3.1. Conventional PFM

The PFM has been widely adopted to model fracture propagation in solids, as pioneered by Francfort and Marigo (1998) and Bourdin et al. (2000). The core principle involves the minimization of the total energy function, which comprises strain energy and a regularized formulation for Griffith's fracture energy. Unlike sharp-crack representations, PFM employs a diffused damage zone, characterized by a phase-field variable ϕ, to approximate crack interfaces. This is achieved through a regularization scheme that replaces the surface integral over the crack Γ with a volumetric integral: $\int_\Gamma \mathrm{d}\Gamma \approx \int_\Omega \gamma(\phi, \nabla\phi)\mathrm{d}V$. $\gamma(\phi, \nabla\phi)$ denotes the crack density function. ϕ quantifies the material damage ($\phi = 0$ indicates intact materials and $\phi = 1$ indicates fully broken materials). The diffused damage zone occurs when the phase field varies between these two values. This variational approach ensures accurate fracture energy characterization near crack tips. In the absence of thermal effects, the internal potential energy $\Psi^{\mathrm{in}}(\boldsymbol{u}, \phi)$ consists of strain energy and fracture energy:

$$\Psi^{\mathrm{in}}(\boldsymbol{u}, \phi) = \underbrace{\int_\Omega \varphi(\boldsymbol{\varepsilon}, \phi)\mathrm{d}V}_{\text{strain energy}} + \underbrace{\int_\Omega G_c \gamma(\phi, \nabla\phi)\mathrm{d}V}_{\text{fracture energy}} \tag{2}$$

where $\varphi(\boldsymbol{\varepsilon}, \phi)$ is the strain energy density, G_c is the critical energy release rate, $\boldsymbol{u}$ is the displacement vector, $\boldsymbol{\varepsilon}$ is the strain tensor (given by $\boldsymbol{\varepsilon} = \nabla^{\mathrm{sym}}\boldsymbol{u}$), and Ω is the computational domain.

In the PFM, material degradation due to damage is modeled via a monotonic degradation function $g(\phi)$. Since the conventional PFM does not distinguish the formulation of crack driving energy, this function quantifies the reduction in strain energy storage capacity due to damage, which is expressed by the following relationship:

$$\varphi(\boldsymbol{\varepsilon}, \phi) = g(\phi)\varphi_0(\boldsymbol{\varepsilon}) \tag{3}$$

The formulation of $g(\phi)$ should satisfy the following conditions: (1) $\mathscr{C}^1$ continuity and monotonicity and (2) boundary conditions ($\left.\frac{\partial g(\phi)}{\partial \phi}\right|_{\phi=1} = 0$, $g(\phi)|_{\phi=0} = 1$, and $g(\phi)|_{\phi=1} = 0$). A typical quadratic formulation $g(\phi) = (1-\phi)^2 + \kappa$ is used, with $\kappa = 1 \times 10^{-9}$, ensuring numerical stability in fully fractured state. The elastic strain energy $\varphi_0(\boldsymbol{\varepsilon})$ is defined as

$$\varphi_0(\boldsymbol{\varepsilon}) = \frac{1}{2}\lambda(\mathrm{tr}[\boldsymbol{\varepsilon}])^2 + u\boldsymbol{\varepsilon} : \boldsymbol{\varepsilon} \tag{4}$$

where λ and u are the Lamé constants of undamaged materials, and $\mathrm{tr}[\boldsymbol{\varepsilon}]$ indicates the trace of the stain tensor $\boldsymbol{\varepsilon}$.

The crack density function $\gamma(\phi, \nabla\phi)$ incorporates the gradient term of the phase field for geometric regularization:

$$\gamma(\phi, \nabla\phi) = \frac{1}{2\ell}\left(\phi^2 + \ell^2 \nabla\phi \cdot \nabla\phi\right) \tag{5}$$

where ℓ is the characteristic length scale which controls the width of the diffused crack band.

The system is additionally subjected to external loading conditions comprising: body force $\boldsymbol{b}$ distributed throughout the domain Ω and surface tractions $\boldsymbol{t}$ applied on the Neumann boundary $\partial\Omega^t$. The external work Ψ^{ext}, which represents the energy contribution by the applied loads, is given by

$$\Psi^{\mathrm{ext}}(\boldsymbol{u}) = \int_\Omega \boldsymbol{b} \cdot \boldsymbol{u}\mathrm{d}\Omega + \int_S \boldsymbol{t} \cdot \boldsymbol{u}\mathrm{d}S \tag{6}$$

Therefore, the total energy of the system Π is

$$\Pi = \Psi^{\mathrm{in}}(\boldsymbol{u}, \phi) - \Psi^{\mathrm{ext}}(\boldsymbol{u}) \tag{7}$$

Applying the divergence theorem to the variational minimization of Π yields the following mechanical balance equation and phase-field governing equation:

$$\left.\begin{aligned} &\mathrm{div}\boldsymbol{\sigma} + \boldsymbol{b} = \boldsymbol{0} \quad (\text{in } \Omega) \\ &g'(\phi)\varphi_0(\boldsymbol{\varepsilon}) - G_c\ell\Delta\phi + \frac{G_c}{\ell}\phi = 0 \quad (\text{in } \Omega) \end{aligned}\right\} \tag{8}$$

where Δ is the Laplace operator, denoted as $\Delta = \nabla\nabla$.

With boundary conditions:

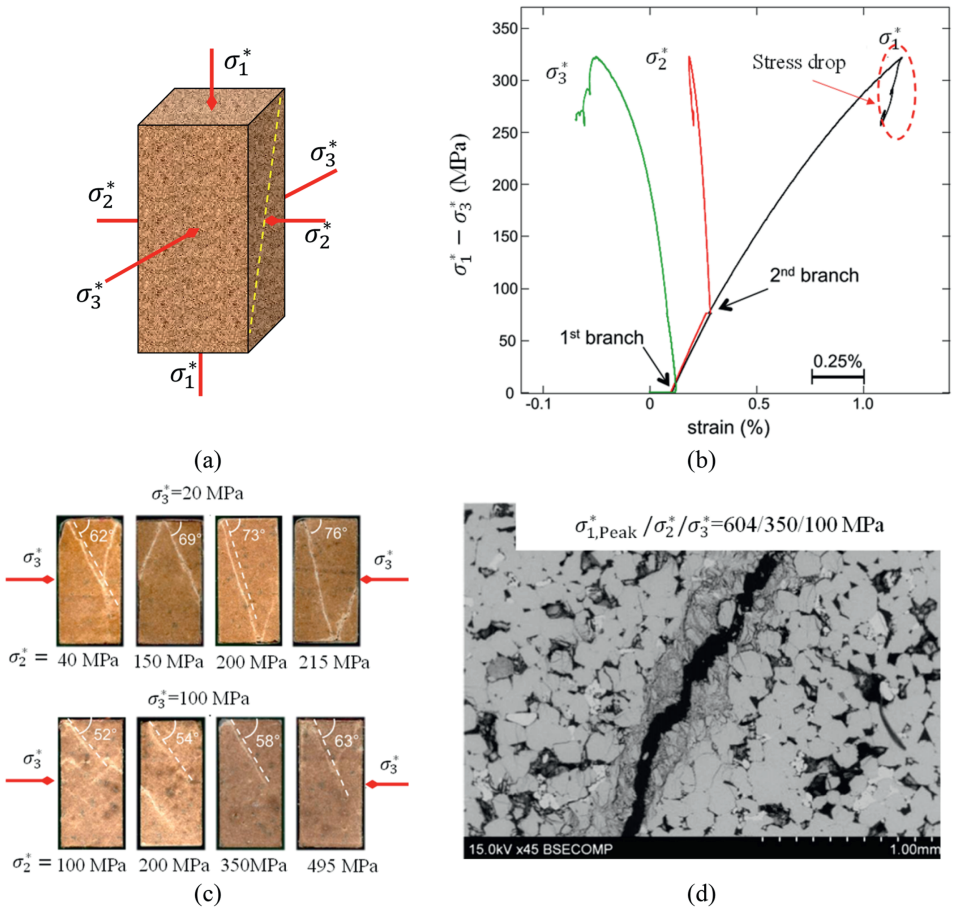

Fig. 2. The TTC test results of Coconino sandstone: (a) Sample, (b) Typical stress-strain curves under $\sigma_3^* = 50$ MPa and $\sigma_2^* = 125$ MPa, (c) Failure modes, and (d) SEM micrograph of the failure-plane zone in σ_1^*-σ_3^* sections. The above test results were collected from the literature (Ma and Haimson, 2016).

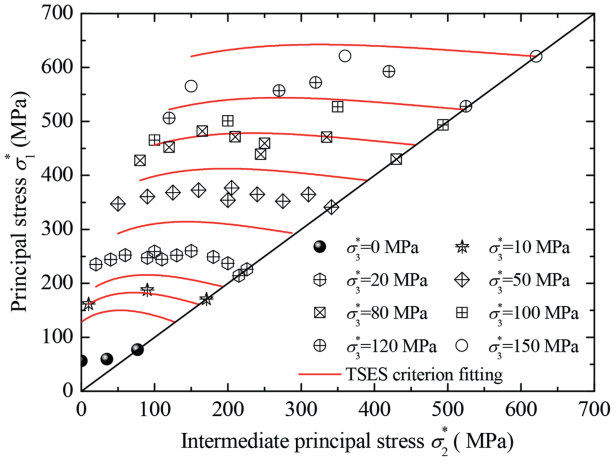

Fig. 3. Validity of the TSES criterion by comparing between fitting results and experimental strengths.

$$\left.\begin{aligned} &\boldsymbol{u} = \overline{\boldsymbol{u}} && (\text{on } \partial\Omega^u)\\ &\boldsymbol{\sigma}\cdot\boldsymbol{n} - \boldsymbol{t} = \boldsymbol{0} && (\text{on } \partial\Omega^t)\\ &\nabla\phi\cdot\boldsymbol{n} = \boldsymbol{0} && (\text{on } \partial\Omega) \end{aligned}\right\} \tag{9}$$

To prevent crack healing, Miehe et al. (2010a) introduced a history-field variable $\mathscr{H}$:

$$\mathscr{H} = \max_{0\le t\le T}\{\varphi_0(\boldsymbol{\varepsilon})\} \tag{10}$$

where t is the current time step and T indicates the duration of history. This substitution ensures damage irreversibility during the complete loading history by tracking the maximum attained elastic strain energy.

3.2. New compressive-shear crack driving energy

The PFM simulates damage evolution through a driving energy functional, whose mathematical formulation critically determines the method's accuracy in modeling fracture propagation. In conventional PFM implementations, the total strain energy serves as the undifferentiated driving force for fracture. While this approach effectively reproduces Mode-I (tensile) fracture in homogeneous solids, it fails to capture the unilateral effects of rock-like materials. Recent methodological developments have addressed this limitation through strain energy decomposition techniques, notably the VD and SD methods (Bian et al., 2024; Liu et al., 2022). These advancements enable separate treatment of tensile and compressive strain energy components, significantly expanding PFM's applicability to rock mechanics problems. However, current implementations still face fundamental challenges in fully characterizing the complex mechanical behavior of rock materials, which exhibit: (1) intrinsic heterogeneity from interlocking mineral grains with frictional properties; (2) cementation effects that enhance shear strength through cohesive bonding and frictional

resistance; and (3) mode-dependent fracture energy with distinct critical release rates for different crack types. These material complexities have motivated the development of advanced mixed-mode PFM frameworks that incorporate decomposed driving energies for tensile, tensile-shear, and compressive-shear cracks (Bryant and Sun, 2018; Spetz et al., 2021; Wang et al., 2024; Zhang et al., 2017a). To properly account for these energy decomposition effects, the standard phase-field governing equation in Eq. (8) requires corresponding modifications that reflect the distinct fracture modes through mode-dependent critical energy release rates, as shown below:

$$g'(\phi)\left(\frac{\varphi_+^{\mathrm{I}}}{G_{\mathrm{cI}}^+}+\frac{\varphi_+^{\mathrm{II}}}{G_{\mathrm{cII}}^+}+\frac{\varphi_-}{G_{\mathrm{c}}^-}\right)-\ell\Delta\phi+\frac{1}{\ell}\phi=0 \tag{11}$$

where G_{cI}^+ refers to the critical energy release rate for the pure tensile condition, G_{cII}^+ represents the critical energy release rate for the tensile-shear condition, and G_{c}^- indicates the critical energy release rate for the compressive-shear condition. The symbols φ_+^{I}, φ_+^{II} and φ_- represent the elastic strain energies associated with tension, tension-shear, and compressive-shear conditions, respectively.

For tensile conditions ($\mathrm{tr}[\boldsymbol{\varepsilon}]>0$), both VD and SD methods yield combined driving energies φ_+^{I} and φ_+^{II} that govern fracture initiation and propagation.

$$\varphi_+^{I}=\frac{1}{2}\lambda'\langle\mathrm{tr}[\boldsymbol{\varepsilon}]\rangle^2 \tag{12a}$$

$$\varphi_+^{II}=(1-\vartheta)u\boldsymbol{\varepsilon}_{\mathrm{dev}}:\boldsymbol{\varepsilon}_{\mathrm{dev}}+\vartheta u\boldsymbol{\varepsilon}^+:\boldsymbol{\varepsilon}^+ \tag{12b}$$

where the symbol $\langle\cdot\rangle$ denotes the Macaulay bracket, taking the form $\langle x\rangle=(x+|x|)/2$; λ' equals $k-\frac{2\vartheta}{3}u$; k and u are the bulk modulus and the shear modulus of the undamaged material, respectively; $\boldsymbol{\varepsilon}_{\mathrm{dev}}$ is the deviatoric strain tensor and $\boldsymbol{\varepsilon}^+$ is the positive principal strain; and ϑ is a coupling parameter ranging from 0 to 1.

Thus, the history-field variables $\mathscr{H}_+^{\mathrm{I}}$ and $\mathscr{H}_+^{\mathrm{II}}$ track the maximum value in the current history, as follows:

$$\mathscr{H}_+^{\mathrm{I}}=\max_{0\le t\le T}\left\{\varphi_+^{\mathrm{I}},\mathscr{H}_+^{\mathrm{I}}\Big|_{(t-1)}\right\} \tag{13a}$$

$$\mathscr{H}_+^{\mathrm{II}}=\max_{0\le t\le T}\left\{\varphi_+^{\mathrm{II}},\mathscr{H}_+^{\mathrm{II}}\Big|_{(t-1)}\right\} \tag{13b}$$

where $\mathscr{H}_+^{\mathrm{I}}\Big|_{(t-1)}$ and $\mathscr{H}_+^{\mathrm{II}}\Big|_{(t-1)}$ are the maximum tensile driving force and tensile-shear driving force in the previous step, respectively.

In analyzing the compressive-shear failure of rock-like materials, it is essential to consider frictional effects and acknowledge that only a portion of the total energy contributes to compressive-shear crack damage. Therefore, a fraction of the energy must be suppressed when regulating crack propagation. The cohesion serves a dual role in compressive-shear failure mechanisms: it resists material failure while simultaneously dissipating the compressive-shear driven energy that would otherwise drive crack growth. Crucially, the strength criterion is adopted as the initiation threshold for phase-field compressive-shear damage, ensuring that the compressive-shear energy accumulation begins from zero. To rigorously capture the coupled evolution of compressive-shear damage and strength degradation, a reformulated 3D shear energy $w_{\mathrm{s}}^{\mathrm{d}}$ is derived from Eq. (A.15) to serve as the updated crack driving force.

$$w_{\mathrm{s}}^{\mathrm{d}}=\frac{3+3\tan^2\theta-4\sqrt{3}\tan\theta\sin\varphi}{4Gg(\phi)\cos^2\varphi\left(1-\sqrt{3}\tan\theta\sin\varphi\right)}\langle\mathscr{F}_{\mathrm{p}}\rangle\mathscr{F}_{\mathrm{p}} \tag{14}$$

where $\mathscr{F}_{\mathrm{p}}$ is an enriched strength criterion designed incorporating strain hardening and softening behaviors by explicitly accounting for the damage-induced degradation of cohesion. The functional form of $\mathscr{F}_{\mathrm{p}}$ is given by

$$\mathscr{F}_{\mathrm{p}}=p\sin\varphi+\frac{q}{\sqrt{3}}\cos\theta-\frac{q}{3}\sin\theta\sin\varphi-\eta g(\phi) \tag{15}$$

The compressive-shear energy exhibits dual dependence on stress components: it is constrained by mean stress while being enhanced by generalized shear stress in the above equation. Crucially, the synergistic coupling between these stress components plays a governing role in compressive-shear damage evolution. Experimental observations from CTC tests on rock-like materials consistently demonstrate that increasing deviatoric stress initiates and propagates cracks while activating additional damage mechanisms. This energy-based fracture propagation theory remains consistent with fundamental physical principles. The proposed framework advances current methodologies by effectively incorporating critical parameters including the Lode angle and frictional effects for accurate crack propagation characterization under TTC stress conditions. The TSES criterion serves dual purposes: (1) identifying compressive-shear crack initiation, and (2) detecting shear slip phenomena. Thus, it provides a fundamental threshold for determining when compressive-shear crack driving energy should be considered. To enforce the irreversibility condition of crack evolution, the history-field variable $\mathscr{H}_-$ is mathematically defined as

$$\mathscr{H}_-=\max_{0\le t\le T}\left\{w_{\mathrm{s}}^{\mathrm{d}},\mathscr{H}_-|_{(t-1)}\right\} \tag{16}$$

where $\mathscr{H}_-|_{(t-1)}$ represents the maximum value of the cracking driven force in all the previous step.

The interaction between different crack types during rock fracture processes plays a critical role in numerical simulations. Accurately capturing this coupled fracture behavior is essential for realistic modeling. To address multiple cracks interactions, we propose a modified formulation of $\mathscr{H}/G_{\mathrm{c}}$ in Eq. (17), which enables a continuous transition between mixed fracturing modes:

$$g'(\phi)\left(\frac{\mathscr{H}_+^{\mathrm{I}}}{G_{\mathrm{cI}}^{+,*}}+\frac{\mathscr{H}_+^{\mathrm{II}}}{G_{\mathrm{cII}}^{+,*}}+\frac{\mathscr{H}_-}{G_{\mathrm{c}}^{-,*}}\right)-\ell\Delta\phi+\frac{1}{\ell}\phi=0 \tag{17}$$

where the definitions of $G_{\mathrm{cI}}^{+,*}$, $G_{\mathrm{cII}}^{+,*}$, and $G_{\mathrm{c}}^{-,*}$ are defined as

$$G_{\mathrm{cI}}^{+,*}=G_{\mathrm{cII}}^+ +\left(G_{\mathrm{cI}}^+-G_{\mathrm{cII}}^+\right)\left(\frac{\mathscr{H}_+^{\mathrm{I}}}{\mathscr{H}_+^{\mathrm{I}}+\mathscr{H}_+^{\mathrm{II}}+\mathscr{H}_-}\right)^{\zeta} \tag{18a}$$

$$G_{\mathrm{cII}}^{+,*}=G_{\mathrm{cI}}^+ +\left(G_{\mathrm{cII}}^+-G_{\mathrm{cI}}^+\right)\left(\frac{\mathscr{H}_+^{II}}{\mathscr{H}_+^{\mathrm{I}}+\mathscr{H}_+^{\mathrm{II}}+\mathscr{H}_-}\right)^{\xi} \tag{18b}$$

$$G_{\mathrm{c}}^{-,*}=\chi\sqrt{\left(G_{\mathrm{cI}}^{+,*}\right)^2+\left(G_{\mathrm{cII}}^{+,*}\right)^2} \tag{18c}$$

where ζ, ξ, and χ are control parameters governing the energy release rate.

3.3. Constitutive model

The evolution of the phase field is intrinsically linked to the degradation of material mechanical properties. This mechanical process can be effectively characterized through a constitutive model incorporating damage degradation functions. In this study, the constitutive behavior of rock materials represents an elastic damage problem governed by phase-field evolution. Importantly, due to the unilateral effect, rock materials exhibit fundamentally different mechanical responses under tensile and compressive stress states. Following the previous study (Cao et al., 2022), the strain energy density φ is formulated by VD and SD contributions through a weighting factor ϑ:

$$\varphi(\boldsymbol{\varepsilon}) = \vartheta\varphi_{\mathrm{SD}}(\boldsymbol{\varepsilon}) + (1-\vartheta)\varphi_{\mathrm{VD}}(\boldsymbol{\varepsilon}) \tag{19}$$

where the SD component of energy $\varphi_{\mathrm{SD}}(\boldsymbol{\varepsilon})$ is defined by $\varphi_{\mathrm{SD}}(\boldsymbol{\varepsilon}) = g(\phi)\left[\frac{1}{2}\lambda[\mathrm{tr}^{+}(\boldsymbol{\varepsilon})]^2 + u\boldsymbol{\varepsilon}^{+}:\boldsymbol{\varepsilon}^{+}\right] + \frac{1}{2}\lambda[\mathrm{tr}^{-}(\boldsymbol{\varepsilon})]^2 + u\boldsymbol{\varepsilon}^{-}:\boldsymbol{\varepsilon}^{-}$ and the VD component of energy $\varphi_{\mathrm{VD}}(\varepsilon)$ is defined by $\varphi_{\mathrm{VD}}(\varepsilon) = g(\phi)\left[\frac{1}{2}k[\mathrm{tr}^{+}(\boldsymbol{\varepsilon})]^2 + u\boldsymbol{\varepsilon}_{\mathrm{dev}}:\boldsymbol{\varepsilon}_{\mathrm{dev}}\right] + \frac{1}{2}k[\mathrm{tr}^{-}(\boldsymbol{\varepsilon})]^2$. $\mathrm{tr}^{+}(\boldsymbol{\varepsilon})$ and $\mathrm{tr}^{-}(\boldsymbol{\varepsilon})$ represent the positive and negative parts of the strain tensor trace, respectively. The weighting parameter ϑ enables flexible adaptation between the VD and SD approaches.

The constitutive relationship is derived as

$$\boldsymbol{\sigma} = \frac{\partial\varphi}{\partial\boldsymbol{\varepsilon}} = g(\phi)\boldsymbol{\sigma}_{\mathrm{d}}^{\mathrm{eff}} + \boldsymbol{\sigma}_{\mathrm{o}}^{\mathrm{eff}} \tag{20}$$

where $\boldsymbol{\sigma}_{\mathrm{d}}^{\mathrm{eff}}$ represents the phase-field-affected degraded stress component, while $\boldsymbol{\sigma}_{\mathrm{o}}^{\mathrm{eff}}$ corresponds to the unaffected stress portion. The effective stresses are decomposed into

$$\boldsymbol{\sigma}_{\mathrm{d}}^{\mathrm{eff}} = \lambda'\mathrm{tr}^{+}(\boldsymbol{\varepsilon})\boldsymbol{\delta} + 2(1-\vartheta)u\boldsymbol{\varepsilon}_{\mathrm{dev}} + 2\vartheta u\boldsymbol{\varepsilon}^{+} \tag{21a}$$

$$\boldsymbol{\sigma}_{\mathrm{o}}^{\mathrm{eff}} = \lambda'\mathrm{tr}^{-}(\boldsymbol{\varepsilon})\boldsymbol{\delta} + 2\vartheta u\boldsymbol{\varepsilon}^{-} \tag{21b}$$

The degradation of material mechanical properties induced by phase-field evolution can be characterized through partial deterioration of elastic stiffness. The resulting damaged stiffness tensor $\mathbb{C}^{\mathrm{d}}$, accounting for phase-field effects, is derived as

$$\begin{aligned}\mathbb{C}^{\mathrm{d}} &= \frac{\partial\boldsymbol{\sigma}}{\partial\boldsymbol{\varepsilon}} = \lambda'\left\{[1-\phi H(\mathrm{tr}(\boldsymbol{\varepsilon}))]^2 + \kappa\right\}\boldsymbol{\delta}\otimes\boldsymbol{\delta} + \\ &2(1-\vartheta)ug(\phi)\mathbb{K} + 2\vartheta u\left\{\left[(1-\phi)^2 + \kappa\right]\mathbb{P}^{+} + \mathbb{P}^{-}\right\}\end{aligned} \tag{22}$$

where $\mathbb{P}^{+}$ and $\mathbb{P}^{-}$ are the fourth-order projection tensors, and $H(\cdot)$ denotes the Heaviside step function. Based on previous study of SD (Miehe, 1998), the projection tensors $\mathbb{P}^{+}$ and $\mathbb{P}^{-}$ are explicitly defined as follows:

$$\begin{aligned}P_{ijkl}^{+} &= \sum_{a=1}^{3}\sum_{b=1}^{3} H(\varepsilon_a)\delta_{ab}n_{ai}n_{aj}n_{bk}n_{bl} + \\ &\sum_{a=1}^{3}\sum_{b\neq a}^{3}\frac{1}{2}\frac{\langle\varepsilon_a\rangle_{+} - \langle\varepsilon_b\rangle_{+}}{\varepsilon_a - \varepsilon_b}n_{ai}n_{bj}(n_{ak}n_{bl} + n_{bk}n_{al})\end{aligned} \tag{23a}$$

$$\begin{aligned}P_{ijkl}^{-} &= \sum_{a=1}^{3}\sum_{b=1}^{3} H(-\varepsilon_a)\delta_{ab}n_{ai}n_{aj}n_{bk}n_{bl} + \\ &\sum_{a=1}^{3}\sum_{b\neq a}^{3}\frac{1}{2}\frac{\langle\varepsilon_a\rangle_{-} - \langle\varepsilon_b\rangle_{-}}{\varepsilon_a - \varepsilon_b}n_{ai}n_{bj}(n_{ak}n_{bl} + n_{bk}n_{al})\end{aligned} \tag{23b}$$

4. Numerical implementation and validation of PFM

PFM has been successfully implemented across various numerical frameworks, including the finite element method (FEM) (Miehe et al., 2010b; Molnár and Gravouil, 2017), materials point method (MPM) (Kakouris and Triantafyllou, 2018), smooth particle hydrodynamics (SPH) (Zhou et al., 2023), and numerical manifold method (NMM) (Yang et al., 2021). As phase-field fracture modeling naturally encompasses coupled mechanical and damage field interactions, the FEM provides an optimal computational platform due to its inherent ability to solve multi-field problems efficiently. Consequently, extensive computational implementations have been developed using commercial software platforms (Zhou et al., 2018; Wang et al., 2021), open-source packages (Rahaman, 2022; Schneider and Nestler, 2023), and in-house codes (Biner, 2017). For brevity, the detailed finite element formulation of PFM is provided in Appendix B. To enhance the practical applicability of our model for engineering applications, we implement the PFM through user-defined subroutines in Abaqus, specifically employing: a User Material (UMAT) subroutine for constitutive response calculations and a user-defined element (UEL) subroutine for phase-field variable solutions. The implementation utilizes Abaqus's built-in quasi-Newton solution

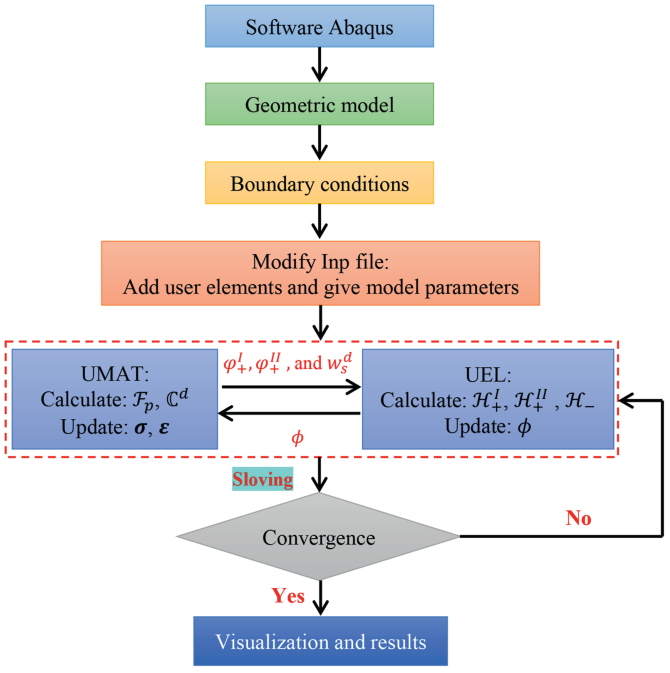

Fig. 4. Flowchart of numerical implementation of the PFM based on the Abaqus platform.

algorithm and adaptive time-stepping scheme to handle nonlinearities. Fig. 4 illustrates the complete finite element implementation workflow, where mechanical variables are efficiently shared between subroutines through common blocks. Each time increment is iteratively solved until the convergence criteria are satisfied, with final results visualized through the software's post-processing capabilities.

To verify numerical accuracy, we first conduct single-element tests where analytical solutions can be derived by neglecting phase-field gradients. For simplicity in analytical verification, we adopt the following parameters: $E = 16.47$ GPa, $\nu = 0.3$, $\vartheta = 0.1$, $\varphi = 46.4°$, $c = 17.39$ MPa, $\ell_c = 1$ mm, $G_{cI}^{+} = G_{cII}^{+} = 0.0055$ kN/mm, $\xi = \zeta = 0$, and $\chi = \sqrt{2}/2$. The elastic and strength parameters are obtained from sandstone tests by Liu (2020). Fig. 5 demonstrates excellent agreement between numerical and analytical results for both uniaxial tension and compression cases. The model successfully reproduces key mechanical responses, including: uniaxial compressive strength (− 87.0 MPa), confining pressure effects, and post-peak residual strength under triaxial conditions.

The modified PFM incorporates seven key parameters ($G_{cI}^{+,*}$, $G_{cII}^{+,*}$, $G_{c}^{-,*}$, ℓ, φ, c and ϑ) that govern simulation results. Existing research demonstrates that material strength exhibits a positive correlation with $G_{cI}^{+,*}$ and $G_{cII}^{+,*}$, while showing an inverse relationship with ℓ. The strength parameter can be directly obtained from triaxial test data, with their impact on fracture propagation analyzed in detail in the subsequent section. The coupling effect of parameter ϑ will be further elucidated through numerical simulations of fissured rock specimens in Section 5.2. In the current analysis, we focus specifically on examining the influence of $G_{c}^{-,*}$ on mechanical response through single-element simulations under uniaxial compression. As defined in Eq. (18c), $G_{c}^{-,*}$ is governed by parameter χ when other fracture energy terms are specified. Notably, the value of G_{c}^{-} increases proportionally with χ. Consequently, our analysis of the influence of $G_{c}^{-,*}$ translates to a sensitivity analysis of χ. For this parametric study, the remaining parameters are held constant with the following values: $E = 16.47$ GPa, $\nu = 0.3$, $\varphi = 46.4°$, $c = 17.39$ MPa, $G_{cI}^{+} = G_{cII}^{+} = 0.0055$ kN/mm, $\vartheta = 0.1$, and $\xi = \zeta = 0$.

The parametric sensitivity analysis presented in Fig. 6 reveals that parameter χ critically governs both the nonlinear hardening behavior during pre-peak loading and the softening characteristics in the post-peak regime. The numerical results demonstrate that increasing the value of χ leads to slower post-peak softening. Fig. 7 presents a systematic investigation of strength parameter effects on the constitutive response, revealing two key observations: (1) both φ and c contribute significantly to peak strength enhancement, and (2) c exerts dominant control over post-peak brittleness. These findings underscore the critical need for rigorous parameter calibration using experimental data to achieve reliable simulation of rock mechanical behavior.

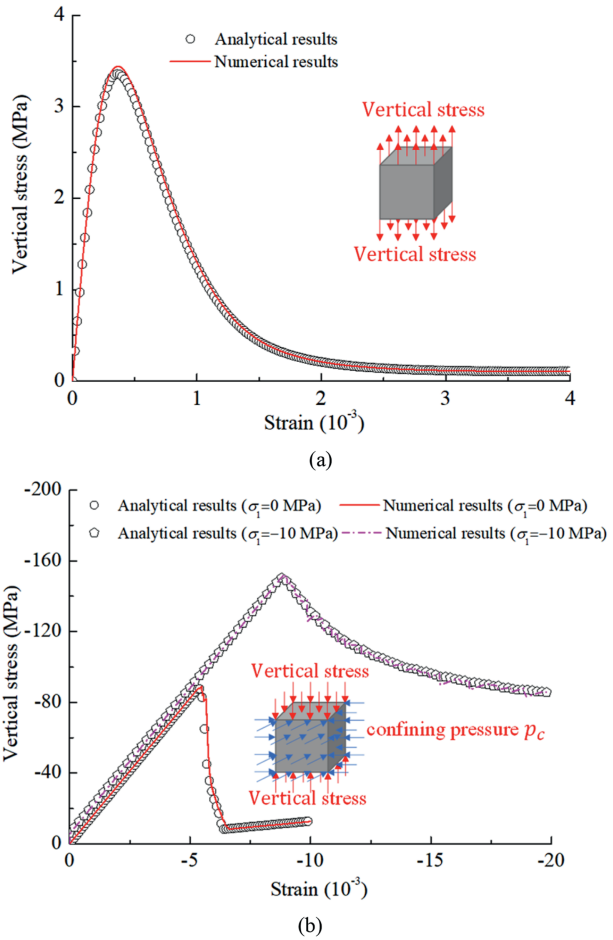

Fig. 5. Comparison between numerical and analytical results of single-element sample: (a) Uniaxial tension, and (b) Triaxial compression.

5. Numerical applications

To demonstrate the 3D crack propagation capabilities of the modified PFM, we present several numerical examples involving rock specimens. One case study investigates single fissured rock specimens with varying inclination angles under uniaxial compression, where numerical results are systematically compared with experimental data to validate the method's accuracy in reproducing crack propagation patterns. Subsequently, the influence of confining pressure on fracture development is examined through numerical modeling of rock specimens containing a pre-existing 45° inclined fissure. Furthermore, the modified PFM is validated by simulating 3D stress rotation in heterogeneous rock.

5.1. Fissured rock with a pre-existing single fissure

The test sample dimensions are 100 mm × 50 mm × 50 mm, containing a single pre-existing fissure along the thickness

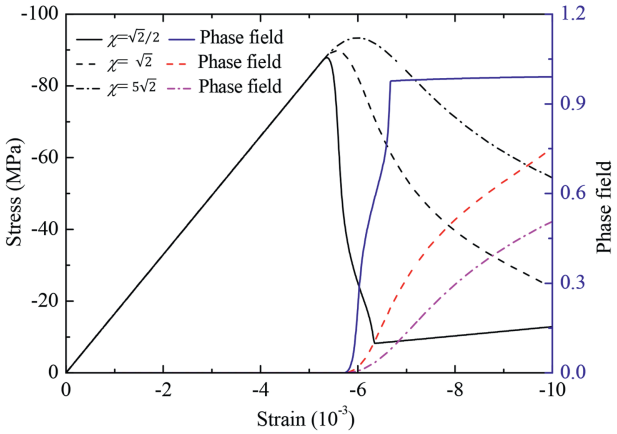

Fig. 6. Sensitivity of the parameter χ.

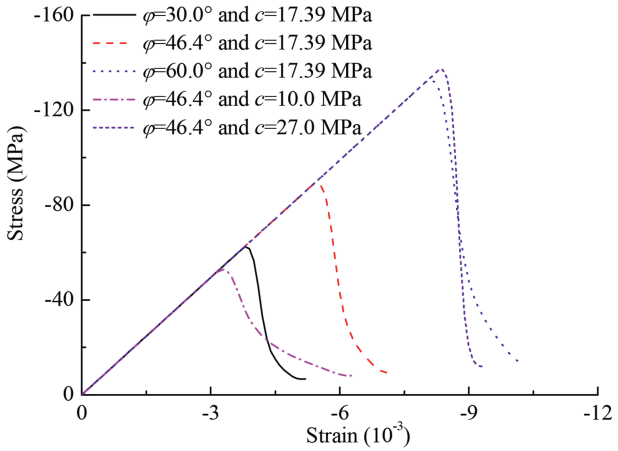

Fig. 7. Sensitivity of the strength parameters.

direction with a length of 14 mm and a width of 2 mm, as documented in Yang et al. (2022). This configuration served as a reference for model validation. The proposed PFM investigates the 3D crack propagation mechanism in fissured rocks simulating the complete failure process. To optimize computational efficiency, only half of the sample thickness is modeled, leveraging symmetry by constraining the mid-surface along the thickness direction. A loading rate of 2 $\times 10^{-3}$ mm/step is applied. Fig. 8 depicts the fissured rock sample, including its boundary conditions and the three characteristic crack types: wing cracks, secondary cracks, and anti-wing cracks. Wing cracks typically indicate tensile fracture mechanisms, whereas secondary cracks arise from shear failure. Given the complex failure behavior of rock materials, a combination of multiple crack types often occurs during propagation.

The samples are discretized using hexahedral elements, with a refined mesh size of 0.5 mm near the pre-existing fissure and a coarser mesh of 1 mm at the sample edges to optimize computational efficiency. The elastic and strength parameters align with those defined in Section 4. In the conventional PFM, the length scale parameter ℓ is typically estimated by $27EG_c/(512\sigma_t^2)$. However, due to the energy splitting approach adopted in the modified

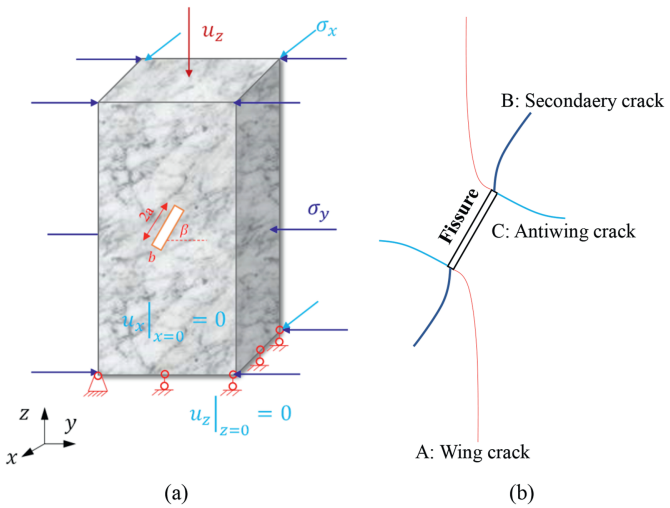

Fig. 8. Boundary conditions of fissured rocks and main crack types: (a) Boundary conditions, and (b) Crack types.

PFM, determining a theoretical value for ℓ becomes challenging. Based on the uniaxial tensile and compressive numerical simulations presented in Section 4, we empirically adopt $\ell = 1.0$ mm for subsequent analyses. The remaining parameters are given as follows under uniaxial compression conditions: $G_{cI}^{+} = 0.0055$ kN/mm, $G_{cII}^{+} = 10\ G_{cI}^{+}$, $\vartheta = 0.1$, $\xi = 2$, $\zeta = 2$, and $\chi = 2$. While direct experimental measurement of fracture energy remains challenging, the values can be approximately calibrated to match the simulated results. It should be noted that fracture energy exhibits stress-state dependency, as demonstrated in recent studies (Verma et al., 2024; Yu et al., 2022). Our findings indicate that while the unified shear energy criterion in PFM enhances strength prediction, its effectiveness, particularly the magnitude of improvement, declines for structures with geometric complexity. This limitation may be addressed in future work by integrating plastic yield criteria. Further improvements to the method will focus on incorporating stress-state-dependent fracture energy. For high confining pressure conditions (e.g. 20 MPa), we select $G_{cI}^{+} = 0.055$ kN/mm to ensure adequate energy distribution.

Fig. 9 illustrates the variations in the load-displacement relationship under different angles in uniaxial compression tests. The results indicate that the pre-existing fissure affects both the macroscopic failure pattern and load-bearing capacity. For $\beta = 0°$, wing cracks initially nucleate at the fissure midpoint and propagate vertically, followed by anti-wing crack development at the fissure tips. At $\beta = 45°$, wing cracks form and propagate during the pre-peak stage, while anti-wing cracks initiate during aggregation and extend in the post-peak stage. This failure pattern, corroborated by CT imaging of fissured sandstone ($\beta = 45°$), is presented in Fig. 11a in the previous work (Yang et al., 2022), with excellent agreement between simulated and experimental crack patterns validating the method's accuracy. The failure mechanism exhibits angular dependence. At $\beta = 60°$, wing cracks form first, followed by secondary cracks propagating from wing crack tips toward the specimen ends. For $\beta = 90°$, wing cracks develop pre-peak but arrest, while anti-wing cracks extend laterally.

Fig. 10 illustrates the variations in the load-displacement relationship of fissured rocks under triaxial compression with a confining pressure of 20 MPa for various inclination angles. The results indicate that confining pressure fundamentally alters failure patterns while enhancing both strength and post-peak ductility, except for $\beta = 90°$. A key observation is the confining pressure-induced shift in anti-wing crack nucleation, which moves from the prefabricated crack tip toward its center. Numerical simulations identify anti-wing cracks as the dominant failure mode under confinement, with suppressed tensile crack propagation near pre-existing crack vertices (comparative analysis between Figs. 9 and 10). The pronounced crack widening observed under confinement further confirms the transition to Compressive-shear dominated failure mechanisms. These findings show excellent agreement with the CT imaging of $\beta = 45°$ fissured sandstone in Fig. 11b from the work (Yang et al., 2022).

Quantitative validation is also performed through peak strength analysis, with Fig. 12 demonstrating strong correlation between simulated and experimental strength values. This agreement confirms the modified PFM's predictive capability for confined fissured rock behavior.

5.2. Influence of parameter ϑ

The parameter ϑ controls the strain energy decomposition scheme, playing a pivotal role in governing crack propagation behavior in phase-field simulations. To systematically evaluate its influence on mechanical response and fracture characteristics, we

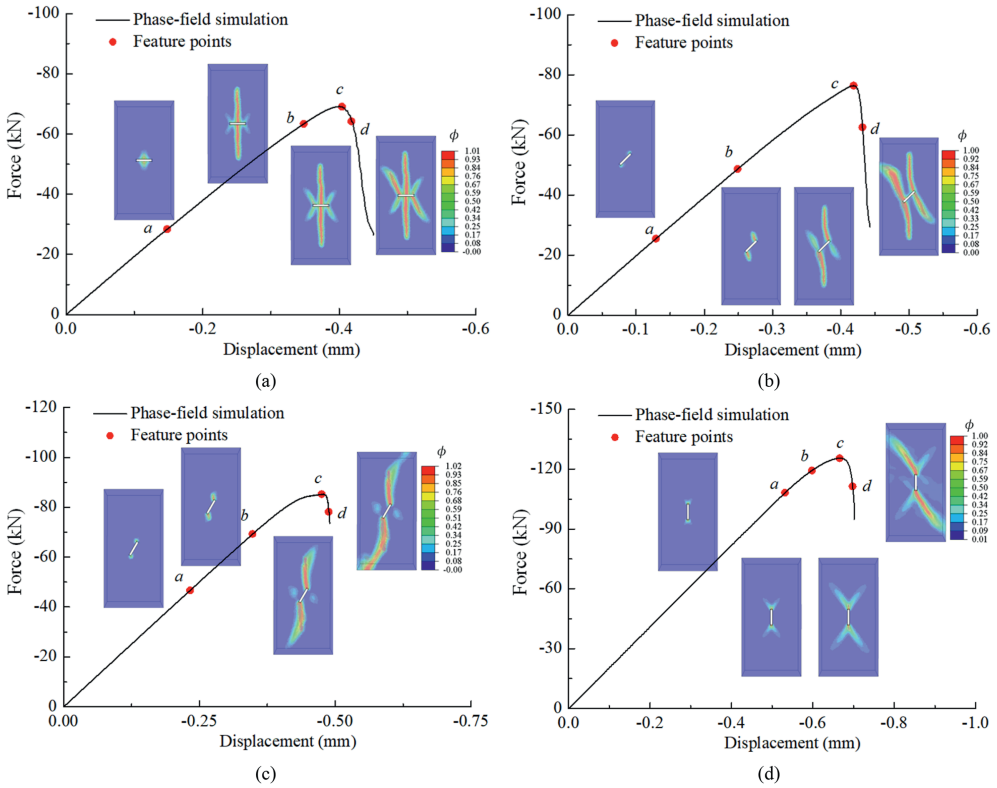

Fig. 9. Loading-displacement curves and crack propagation process in the uniaxial compression condition: (a) $\beta = 0°$, (b) $\beta = 45°$, (c) $\beta = 60°$, and (d) $\beta = 90°$.

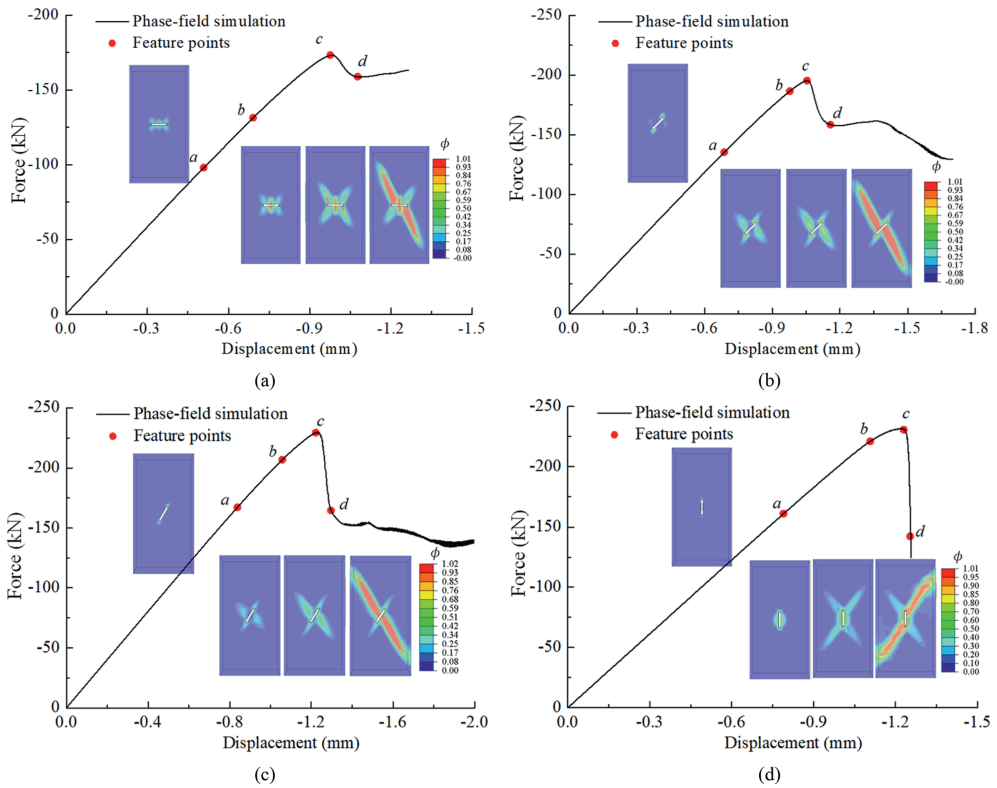

Fig. 10. Load-displacement response and crack evolution under triaxial compression with a confining pressure of 20 MPa: (a) $\beta = 0°$, (b) $\beta = 45°$, (c) $\beta = 60°$, and (d) $\beta = 90°$.

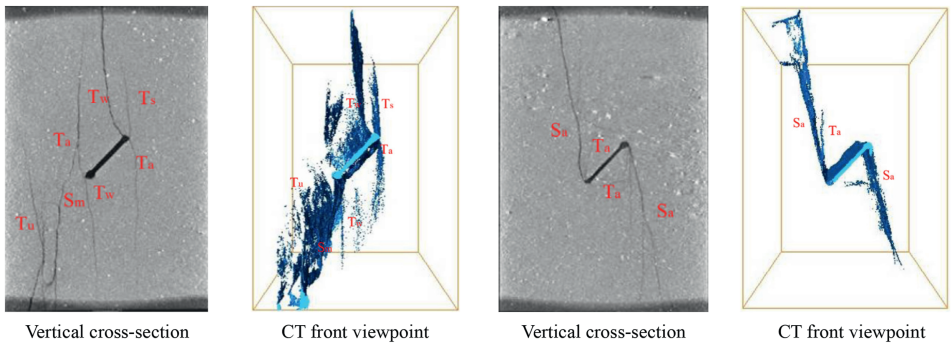

Fig. 11. Failure mode and 3D CT images of fissured sandstone with a single fissure ($\beta = 45°$): (a) $\sigma_x = \sigma_y = 0$ MPa, and (b) $\sigma_x = \sigma_y = -20$ MPa (Yang et al., 2022).

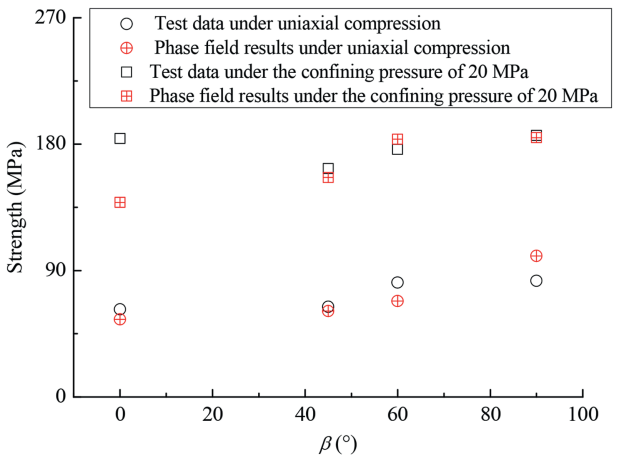

Fig. 12. Strength comparison results between test data and phase-field simulation under uniaxial and triaxial compression conditions.

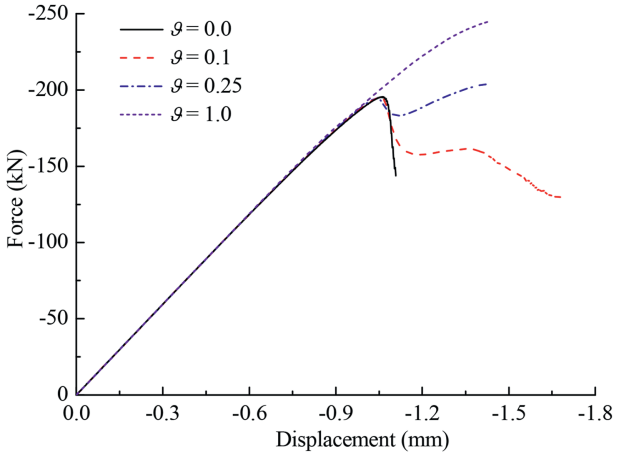

Fig. 13. Influence of parameter ϑ on the loading vs. displacement response.

conducted numerical simulations on a fissured rock specimen ($\beta = 45°$) under triaxial compression with a confining pressure of 20 MPa, examining four distinct values of ϑ. Notably, the unified method reverts to the VD method when $\vartheta = 0.0$, while it reverts to the SD method when $\vartheta = 1.0$. The intermediate value ($0 < \vartheta < 1$) represents a coupled formulation of these two decomposition schemes. Fig. 13 presents the loading-displacement responses under various ϑ with a confining pressure of 20 MPa. The simulation results demonstrate enhanced strength and improved ductility with increasing ϑ. Corresponding fracture patterns in Fig. 14 reveal a distinct ϑ dependence, where crack aperture progressively widens with higher ϑ values. This phenomenon stems from the fundamental assumption of the SD method, which excludes compressive strain contributions to damage evolution. Consequently, damaged regions retain higher load-bearing capacity, an effect that becomes increasingly pronounced at larger ϑ values.

5.3. True 3D stress effect of heterogeneous rock materials

Stress rotation phenomena within fractured damage zones are well-documented (Faulkner et al., 2006), necessitating investigation of the modified PFM capability in simulating crack propagation under true 3D stress conditions. This represents a critical aspect of model validation. In this study, we conceptualize the rock microstructure as comprising three distinct components: block aggregates, matrix material, and interfacial transition zones (ITZs), where the ITZs are explicitly modeled as the structurally weakest constituent. The computational domain measures 50 mm × 50 mm × 50 mm, containing randomly distributed elliptical aggregates (20% by volume) with diameters ranging from 3 mm to 5 mm, as illustrated in Fig. 15a. The heterogeneous geometric model is discretized into 300,763 hexahedral elements with a uniform mesh size of 0.75 mm. The boundary conditions are imposed by applying displacement constraints on the left, bottom, and back faces. Stress constraints are imposed on the three opposing lateral faces. The vertical displacement-controlled loading is applied at a constant strain rate of 1×10^{-3}. The prescribed stress path is shown in Fig. 15b. To accentuate heterogeneity effects under these loading conditions, we deliberately amplify the fracture energy contrast between rock aggregates, matrix, and ITZs. All material parameters for the computational model are systematically summarized in Table 1.

Numerical simulations were conducted by progressively increasing σ_x from 0 to − 50 MPa while maintaining a constant σ_y of − 20 MPa. The differential stress-strain curves (Fig. 16) indicate that higher compressive stress σ_x significantly improves both the bearing capacity and deformability. With increasing σ_x, the failure mechanism transitions from brittle fracture to increasingly ductile deformation. Comparative analysis reveals that the intermediate principal stress exerts substantially less influence on peak strength than the minimum principal stress. These numerical observations show remarkable consistency with experimental results from TTC tests reported by Feng et al. (2019).

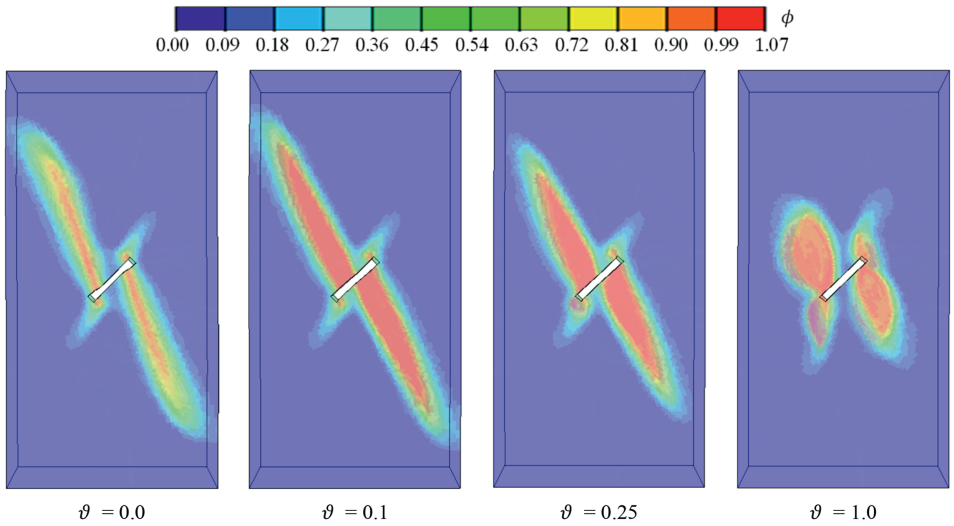

Fig. 14. Influence of parameter ϑ on the crack propagation.

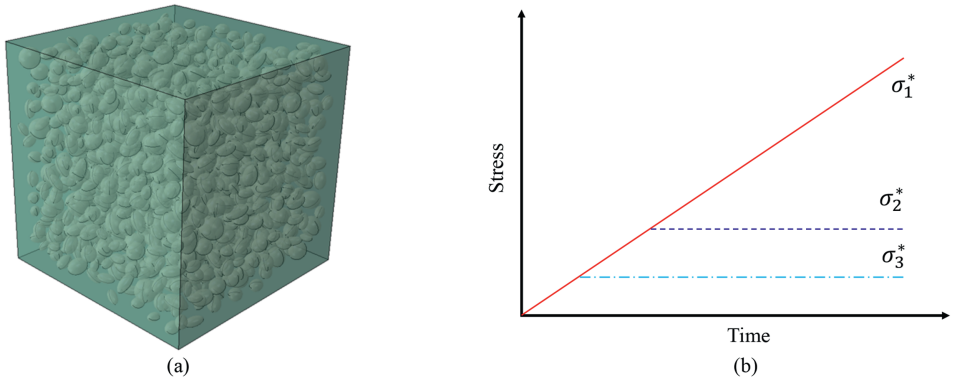

Fig. 15. Geometrical model (a) and stress path in numerical test (b).

Table 1
The required model parameters during the phase field modeling.

Material parameter	Rock aggregate	Matrix	ITZ
E	16.47 GPa	5.65 GPa	1.65 GPa
ν	0.3	0.3	0.3
φ	56.4°	46.4°	26.4°
c	17.39 MPa	8.74 MPa	1.74 MPa
G_{cI}^{+}	55 kN/mm	0.055 kN/mm	0.011 kN/mm
G_{cII}^{+}	550 kN/mm	0.55 kN/mm	0.11 kN/mm
ℓ	1.5 mm	1.5 mm	1.5 mm
ξ	2	2	2
ζ	2	2	2
X	2	2	2

The fracture characteristics under TTC are illustrated in Fig. 17, revealing distinct failure mechanisms compared to CTC conditions. Under TTC conditions, the rock develops predominant shear fractures oriented parallel to the direction of the intermediate principal stress while forming in the plane of the maximum and minimum principal stresses. This produces more localized damage zones compared to the diffuse cracking patterns observed in CTC tests. The fracture plane inclination angle exhibits distinct dependencies on principal stresses: it decreases systematically with increasing minimum principal stress, while showing a positive correlation with intermediate principal stress magnitude. This

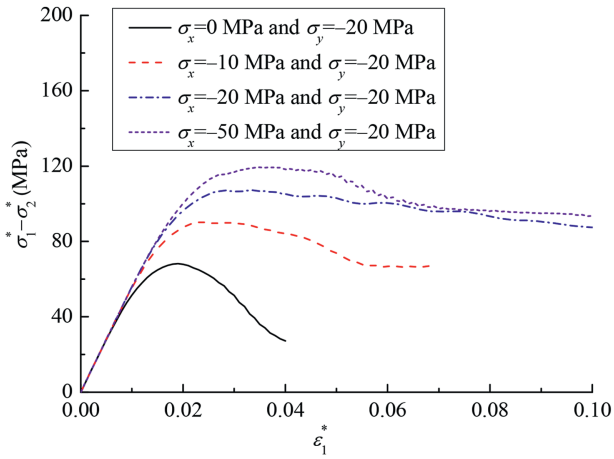

Fig. 16. The differential stress-strain curves under TTC condition.

stress-dependent fracture behavior has been verified through laboratory investigations of various lithologies, including porous sandstone (Ma and Haimson, 2016), amphibolite (Chang and Haimson, 2000), and granite (Feng et al., 2016). These observations demonstrate two fundamental mechanical transitions: (1) a progressive brittle-to-ductile transition driven by the minimum

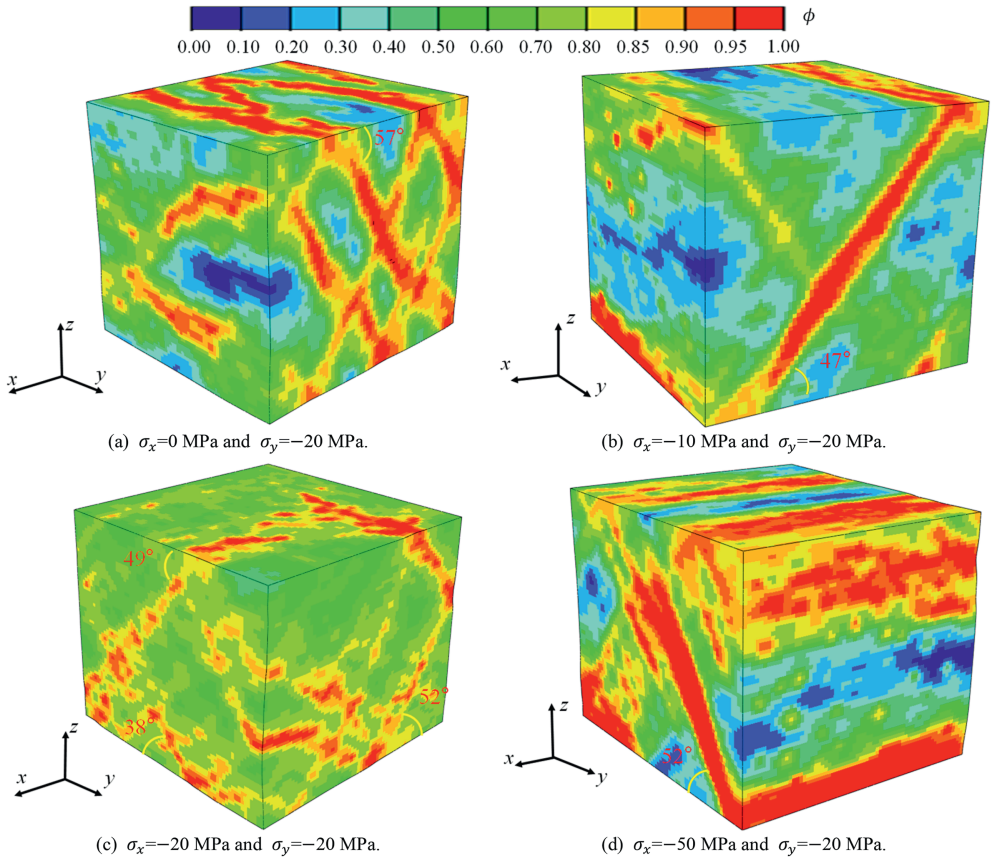

(a) σ_x=0 MPa and σ_y=−20 MPa. (b) σ_x=−10 MPa and σ_y=−20 MPa.

(c) σ_x=−20 MPa and σ_y=−20 MPa. (d) σ_x=−50 MPa and σ_y=−20 MPa.

Fig. 17. Crack distribution of heterogeneous rock under various TTC stress states.

principal stress, and (2) enhanced brittle fracturing associated with elevated intermediate principal stress conditions.

5.4. Discussion

5.4.1. Multiple cracks propagation analysis

Commonly, rock deformation and failure involve complex multiple crack processes, including initiation, propagation, and coalescence. To methodically examine multiple crack propagation based on the simulation results given in Section 5.1, we extract energy and volumetric strain cloud maps (corresponding to the point *d* in Figs. 9 and 10). The phase-field damage driving energy and volumetric strain distributions enable clear differentiation among tensile, tension-shear, and Compressive-shear cracks. A comparative analysis in Fig. 18 illustrates characteristic fracture propagation patterns in rock specimens subjected to varying inclination angles and stress regimes.

Fig. 18a and b presents the comparative fracture characteristics of a single fissured rock specimen ($\beta = 0°$) subjected to uniaxial and triaxial compression (20 MPa confining pressure) conditions, respectively. The uniaxial compression results reveal three distinct crack types, with tensile and tensile-shear cracks emerging as the predominant failure mechanisms. These cracks predominantly localize within the zones of tensile strain concentration. The central vertical cracks exhibit primarily tensile characteristics, whereas tensile-shear cracks initiate at the upper-left and lower-right fissure tips and then propagate toward the specimen boundaries. These fracture patterns are accompanied by localized mixed-mode cracking, comprising tensile, tensile-shear, and compressive-shear components. Notably, compressive-shear cracks do not form a well-defined macroscopic fracture network in the presence of these loading conditions. In contrast, triaxial compression condition induces a fundamentally different fracture regime, where compressive-shear cracks become the dominant failure mode. These cracks initiate at the upper-left and lower-right fissure tips and propagate toward the boundaries. Meanwhile, tensile mixed cracks (i.e. tensile and tensile-shear cracks) develop along the mid-section of the fissure; however, their propagation is substantially constrained, with only limited extension observed due to the inhibitory effect of confining pressure.

Fig. 18c and d illustrates the comparative fracture characteristics of a single-fissured rock specimen ($\beta = 45°$) subjected to uniaxial and triaxial compression (20 MPa confining pressure) conditions, respectively. The uniaxial compression tests reveal tensile-dominated mixed mode cracking as the primary failure mechanism, where persistent compressive stress concentrations promote substantial accumulation of compressive-shear strain energy throughout the failure process. In contrast, triaxial compression conditions induce a distinct failure mode transition, with compressive-shear cracks becoming dominant. Under confinement, tensile-dominated mixed cracks preferentially develop near the upper-right and lower-left regions of the pre-existing fissure, where tensile-shear cracks constitute the predominant fracture type.

Fig. 18e and f demonstrates the fracture characteristics of a single-fissured rock specimen ($\beta = 60°$) under uniaxial and triaxial compression (20 MPa confining pressure) conditions, respectively. The uniaxial compression results reveal that failure is predominantly driven by tensile-dominated mixed-mode fractures

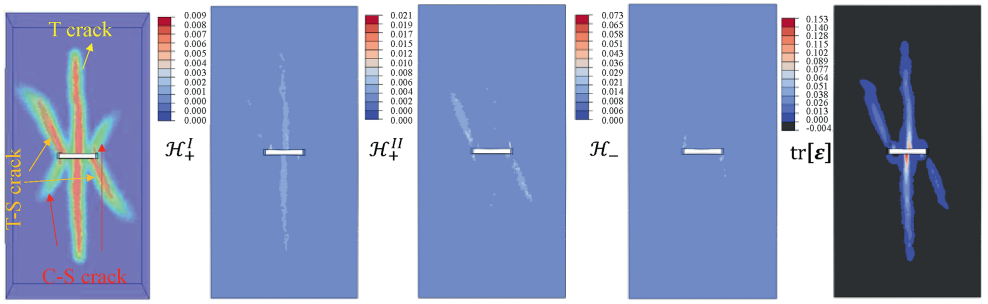

(a) β = 0° under uniaxial compression.

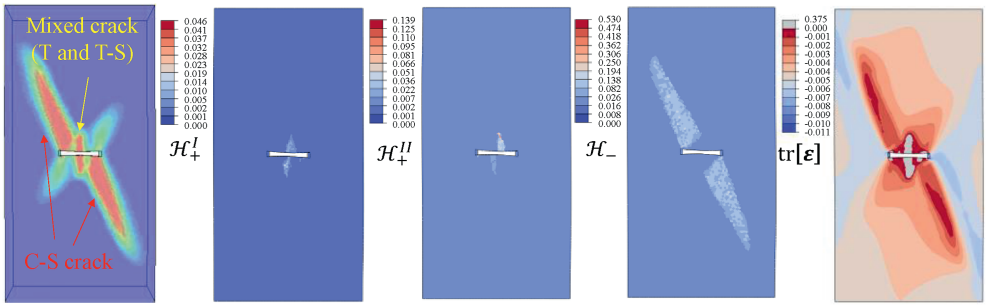

(b) β = 0° under a confining pressure of 20 MPa.

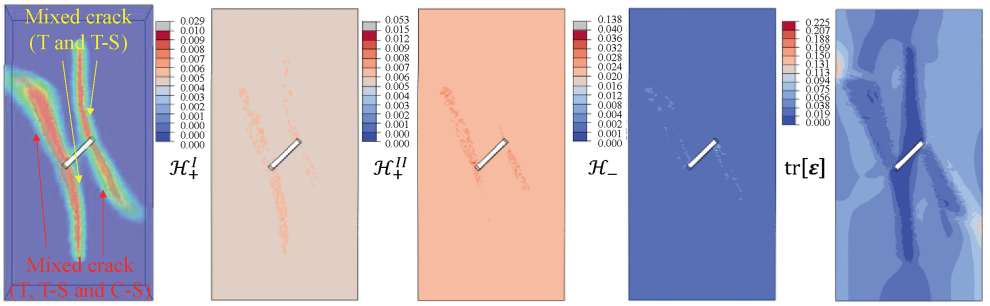

(c) β = 45° under uniaxial compression.

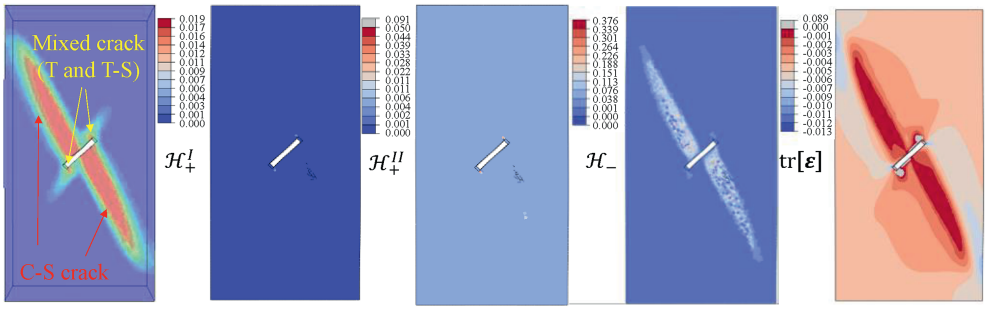

(d) β = 45° under a confining pressure of 20 MPa.

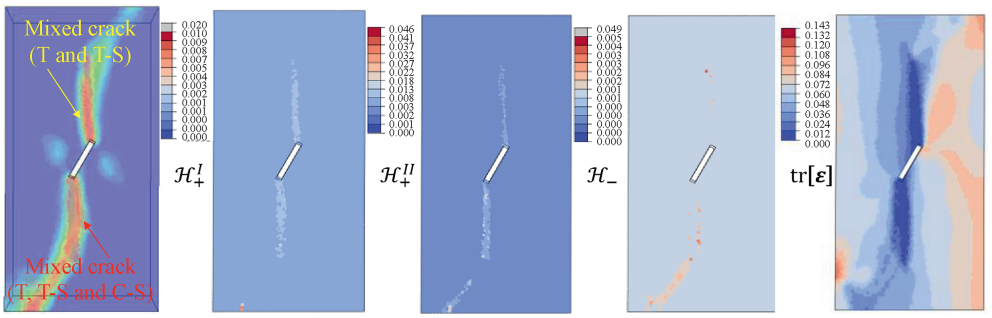

(e) β = 60° under uniaxial compression.

Fig. 18. Multiple cracks distribution of a single fissured rock under uniaxial and TTC condition (The labels T, T-S, and C-S, respectively, denote tensile, tensile-shear, and compressive-shear failure modes).

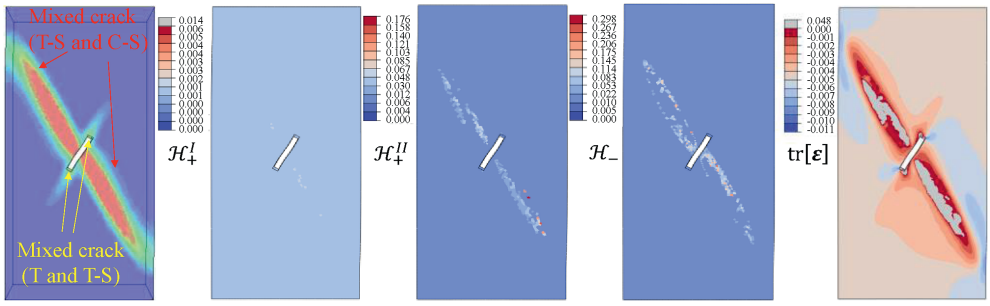

(f) β = 60° under a confining pressure of 20 MPa.

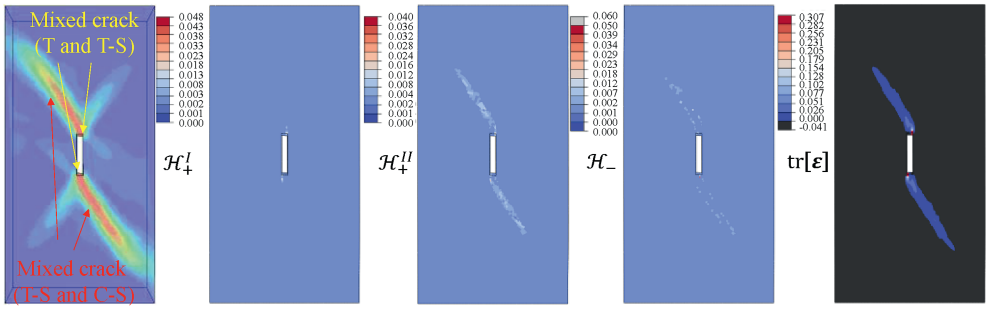

(g) β = 90° under uniaxial compression.

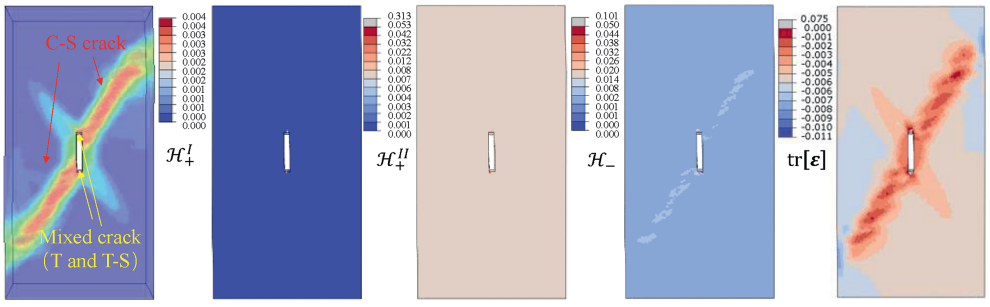

(h) β = 90° under a confining pressure of 20 MPa.

Fig. 18. (*continued*).

(combining tension and tensile-shear mechanisms), while localized Compressive-shear cracks develop in the lower damage zone due to accumulated shear strain energy. Under triaxial confinement, the fracture pattern transitions to a more complex mixed-mode failure, featuring: distributed mixed cracks (tensile-shear and Compressive-shear dominated) along both sides of the specimen and concentrated tensile-dominated mixed fractures (tension and tensile-shear) near pre-existing fissure tips.

Fig. 18g and h presents the fracture characteristics of a single-fissured rock specimen (β = 90°) under uniaxial and triaxial compression (20 MPa confining pressure) conditions, respectively. The uniaxial compression results indicate that multiple crack propagation phenomena are observed. Tensile-dominated mixed cracks (tensile and tensile-shear) initiate at the tips of the pre-existing fissure. Additionally, mixed-mode cracks (tensile-shear and Compressive-shear) develop in the upper-left and lower-right regions of the fissure. In contrast, compressive-shear cracking dominates the failure process, forming a well-defined macroscopic fracture that propagates diagonally from the bottom-left to the top-right of the specimen under triaxial compression. While localized tensile and tensile-shear cracks still initiate at the fissure tips, their propagation is substantially inhibited by the confining pressure, leading to a remarkable reduction in macroscopic fracture development when compared to the uniaxial loading scenario.

In summary, the above work demonstrates that crack propagation in fissured rocks undergoes a fundamental transition from tensile-dominated to shear-driven failure under triaxial compression. The resulting fracture patterns exhibit a strong dependence on fissure inclination angles. Confining pressure plays a dual role: it significantly suppresses tensile crack initiation and propagation while promoting the development of shear-dominated macroscopic fractures. These findings underscore the critical interdependence between stress state and geometric factors in governing rock failure mechanisms.

5.4.2. *Rock failure analysis in true 3D stress condition*

Experimental investigations have demonstrated that the intermediate principal stress significantly influences both rock strength and failure modes. TTC numerical tests reveal that increasing the intermediate principal stress enhances brittle fracture characteristics in rocks. These findings provide a theoretical foundation for optimizing underground cavern design - strategic control management of the intermediate principal stress can effectively mitigate rockburst hazards. Under true 3D stress states, the dominant shear failure plane develops parallel to the orientation of the intermediate principal stress, which representing a critical consideration for support system design.

Crack clusters exhibit preferential growth along in a dominant direction under a non-equal stress conditions (Wang and Xu,

2020), resulting in the stress-induced anisotropic damage of rock materials, even in those that are nominally isotropic. We hypothesize that the intermediate principal stress effect in rock materials arises from this stress-induced anisotropy. Future research will further investigate this phenomenon through two complementary approaches: (1) development of improved constitutive relations and (2) advanced characterization of phase field variables.

The stress redistribution caused by underground excavation demonstrates distinctive spatiotemporal evolution characteristics (Eberhardt, 2001). However, due to the limitations of laboratory test conditions, most existing research has failed to adequately account for the stress rotation effects. This study further highlights the critical need to incorporate 3D stress rotation in simulations of crack propagation behavior. The relationship between fracture energy and stress state is highly complex and resists exact formulation. Current findings suggest this interdependence requires further elucidation through combined theoretical modeling and experimental validation.

6. Conclusions

This study develops a comprehensive PFM that represents an advancement in simulating 3D multiple crack propagation in rock materials. The proposed model innovatively integrates the TSES criterion with conventional strain energy decomposition approaches (VD/SD), enabling explicit differentiation between tensile, tensile-shear, compressive-shear, and mixed-mode fracture mechanisms. Through comprehensive validation against analytical solutions and extensive 3D numerical simulations encompassing both single-fissure specimens and heterogeneous materials, the model demonstrates remarkable capability in capturing stress-state dependent crack propagation patterns and anisotropic damage evolution under polyaxial loading conditions. The key findings reveal that crack propagation in fissured rocks transitions from tensile-dominated to shear-driven failure under triaxial compression, with crack patterns exhibiting a strong dependence on fissure inclination angles.

The modified PFM provides three key improvements for analyzing rock fracture. First, it enables clear mechanical distinction between different fracture types by refining strain energy decomposition. Second, it accurately models shear failure with friction while maintaining compatibility with traditional energy division approaches. Third, when implemented using UMAT/UEL subroutines, it can effectively simulate complex 3D crack patterns. These advancements provide valuable insights for critical engineering applications, such as underground excavation, where accurate prediction of mixed-mode fracture behavior under polyaxial stress conditions are essential.

The key findings indicate significant stress-state effects on fracture patterns, while highlighting important limitations for future research: (i) the necessity to incorporate plasticity mechanisms governing highly confined ductile behavior (e.g. pore collapse and grain crushing), and (ii) the need for improved characterization of anisotropic damage in non-homogeneous stress fields. Addressing these challenges is expected to reconcile laboratory-scale observations with field-scale rock behavior, further establishing PFM as a versatile tool for geomechanical analysis. The present research aims to establish a robust foundation for these future developments, while providing practical improvements for fracture prediction in rock engineering applications.

CRediT authorship contribution statement

Susheng Wang: Writing – review & editing, Writing – original draft, Validation, Software, Methodology, Investigation, Funding acquisition, Conceptualization. **Sheng-Qi Yang:** Writing – review & editing, Validation, Supervision, Methodology, Conceptualization. **Qiang Zhang:** Writing – review & editing, Validation, Supervision, Funding acquisition, Conceptualization. **Changdong Ding:** Writing – review & editing, Validation, Supervision, Methodology. **Qingfu Huang:** Writing – review & editing, Validation, Resources, Methodology, Funding acquisition. **Wanqing Shen:** Writing – review & editing, Validation, Methodology, Investigation, Conceptualization.

Declaration of competing interest

The authors declare that they have no known competing financial interests or personal relationships that could have appeared to influence the work reported in this paper.

Acknowledgments

This study is financially supported by the National Natural Science Foundation of China (Grant No. 52109143), the Open Research Fund of State Key Laboratory of Simulation and Regulation of Water Cycle in River Basin (China Institute of Water Resources and Hydropower Research) (Grant No. IWHR-SKL-KF202305), and the Science and technology project of China Huaneng Group Co., Ltd. (Grant No. HNKJ22-H107).

Appendices A and B. Supplementary data

Supplementary data to this article can be found online at https://doi.org/10.1016/j.jrmge.2025.08.045.

References

Amor, H., Marigo, J.-J., Maurini, C., 2009. Regularized formulation of the variational brittle fracture with unilateral contact: numerical experiments. J. Mech. Phys. Solid. 57 (8), 1209–1229.
Bhattacharya, P., Viesca, R.C., 2019. Fluid-induced aseismic fault slip outpaces pore-fluid migration. Science 364, 464–468.
Bian, P.-L., Qing, H., Yu, T., Schmauder, S., 2024. A novel and simple variationally-consistent phase-field cohesive zone model for mixed-mode fracture. Theor. Appl. Fract. Mech. 130, 104324.
Biner, S.B., 2017. Programming phase-field Modeling. Springer.
Bourdin, B., Francfort, G.A., Marigo, J.-J., 2000. Numerical experiments in revisited brittle fracture. J. Mech. Phys. Solid. 48 (4), 797–826.
Bryant, E.C., Sun, W., 2018. A mixed-mode phase field fracture model in anisotropic rocks with consistent kinematics. Comput. Methods Appl. Math. 342, 561–584.
Cai, M., Hou, P., Zhang, X., Feng, X., 2021. Post-peak stress–strain curves of brittle hard rocks under axial-strain-controlled loading. Int. J. Rock mech. Min. 147, 104921.
Cao, Y., Wang, W., Shen, W., Cui, X., Shao, J., 2022. A new hybrid phase-field model for modeling mixed-mode cracking process in anisotropic plastic rock-like materials. Int. J. Plast. 157, 103395.
Chang, C., Haimson, B., 2000. True triaxial strength and deformability of the German Continental deep drilling Program (KTB) deep hole amphibolite. J. Geophys. Res. Solid Earth 105 (B8), 18999–19013.
Chen, L., Wang, C.P., Liu, J.F., Liu, J., Wang, J., Jia, Y., Shao, J.F., 2015. Damage and plastic deformation modeling of Beishan granite under compressive stress conditions. Rock Mech. Rock Eng. 48 (4), 1623–1633.
Diederichs, M., Kaiser, P., Eberhardt, E., 2004. Damage initiation and propagation in hard rock during tunnelling and the influence of near-face stress rotation. Int. J. Rock Mech. Min. 41 (5), 785–812.
Du, K., Tao, M., Li, X., Zhou, J., 2016. Experimental study of slabbing and rockburst induced by true-triaxial unloading and local dynamic disturbance. Rock Mech. Rock Eng. 49, 3437–3453.
Eberhardt, E., 2001. Numerical modelling of three-dimension stress rotation ahead of an advancing tunnel face. Int. J. Rock Mech. Min. 38 (4), 499–518.
Faulkner, D., Mitchell, T., Healy, D., Heap, M., 2006. Slip on 'weak' faults by the rotation of regional stress in the fracture damage zone. Nature 444 (7121), 922–925.
Fei, F., Choo, J., 2021. Double-phase-field formulation for mixed-mode fracture in rocks. Comput. Methods Appl. Math. 376, 113655.
Feng, Y., Li, J., 2023. A unified regularized variational cohesive fracture theory with directional energy decomposition. Int. J. Eng. Sci. 182, 103773.
Feng, X.-T., Zhang, X., Kong, R., Wang, G., 2016. A novel mogi type true triaxial testing apparatus and its use to obtain complete stress–strain curves of hard

rocks. Rock Mech. Rock Eng. 49 (5), 1649–1662.
Feng, X.-T., Kong, R., Zhang, X., Yang, C., 2019. Experimental study of failure differences in hard rock under true triaxial compression. Rock Mech. Rock Eng. 52 (7), 2109–2122.
Feng, X.-T., Kong, R., Yang, C., Zhang, X., Wang, Z., Han, Q., Wang, G., 2020. A three-dimensional failure criterion for hard rocks under true triaxial compression. Rock Mech. Rock Eng. 53 (1), 103–111.
Francfort, G.A., Marigo, J.-J., 1998. Revisiting brittle fracture as an energy minimization problem. J. Mech. Phys. Solid. 46 (8), 1319–1342.
Gao, H., Zheng, Y., Feng, X., 2007. Study on energy yield criterion of geomaterials. Chin. J. Rock Mech. Eng. 26 (12), 2437–2443 (in Chinese).
Hai, L., Zhang, H., Wriggers, P., Huang, Y.-j., Feng, Y., Junker, P., 2024a. A novel semi-explicit numerical algorithm for efficient 3D phase field modelling of quasi-brittle fracture. Comput. Methods Appl. Math. 432, 117416.
Hai, L., Zhang, H., Wriggers, P., Huang, Y.-j., Zhuang, X.-Y., Xu, S.-L., 2024b. 3D concrete fracture simulations using an explicit phase field model. Int. J. Mech. Sci. 265, 108907.
Kakouris, E., Triantafyllou, S., 2018. Material point method for crack propagation in anisotropic media: a phase field approach. Arch. Appl. Mecharch. Appl. Mech. 88 (1), 287–316.
Li, Z., Zhou, H., Hu, D., Zhang, C., 2020. Yield criterion for rocklike geomaterials based on strain energy and CMP model. Int. J. GeoMech. 20 (3), 04020013.
Li, Z., Shen, Y., Han, F., Yang, Z., 2021. A phase field method for plane-stress fracture problems with tension-compression asymmetry. Eng. Fract. Mech. 257, 107995.
Li, Z., Wang, L., Wang, L., Fan, H., Ren, B., Ding, K., 2024. Study on the evolution of rock fracture under true triaxial intermediate principal stress. Int. J. GeoMech. 24 (1), 04023254.
Liu, X.R., 2020. Study on the Mechanical Behavior and Failure Mechanism of Fissured Rock Under Triaxial Compression. China University of Mining and Technology. PhD Thesis.
Liu, S., Wang, Y., Peng, C., Wu, W., 2022. A thermodynamically consistent phase field model for mixed-mode fracture in rock-like materials. Comput. Methods Appl. Math. 392, 114642.
Ma, X., Haimson, B.C., 2016. Failure characteristics of two porous sandstones subjected to true triaxial stresses. J. Geophys. Res. Solid Earth 121 (9), 6477–6498.
Miehe, C., 1998. Comparison of two algorithms for the computation of fourth-order isotropic tensor functions. Comput. Struct. 66 (1), 37–43.
Miehe, C., Hofacker, M., Welschinger, F., 2010a. A phase field model for rate-independent crack propagation: robust algorithmic implementation based on operator splits. Comput. Methods Appl. Math. 199 (45–48), 2765-277.
Miehe, C., Welschinger, F., Hofacker, M., 2010b. Thermodynamically consistent phase-field models of fracture: variational principles and multi-field FE implementations. Int. J. Numer. Methods Eng. 83 (10), 1273–1311.
Molnár, G., Gravouil, A., 2017. 2D and 3D Abaqus implementation of a robust staggered phase-field solution for modeling brittle fracture. Finite Elem. Anal. Des. 130, 27–38.
Nguyen, G.D., Nguyen, C.T., Nguyen, V.P., Bui, H.H., Shen, L., 2016. A size-dependent constitutive modelling framework for localised failure analysis. Comput. Mech. 58 (2), 257–280.
Ortlepp, W.D., Stacey, T.R., 1994. Rockburst mechanisms in tunnels and shafts. Tunn. Undergr. Space Technol. 9, 59–65.
Perras, M.A., Diederichs, M.S., 2016. Predicting excavation damage zone depths in brittle rocks. J. Rock mech. Geotech. 8 (1), 60–74.
Piska, R., Sivadas, K., Boyina, K., Vuppuluri, A., Chaurasia, A., Parimi, C., Rabczuk, T., 2024. Recent trends in computational damage models: an overview. Theor. Appl. Fract. Mech. 132, 104494.
Rahaman, M.M., 2022. An open-source implementation of a phase-field model for brittle fracture using gridap in julia. Math. Mech. Solid 27 (11), 2404–2427.
Schneider, D., Nestler, B., 2023. Realization of adaptive mesh refinement for phase-field model of thermal fracture within the FEniCS framework. Eng. Fract. Mech. 293, 109676.
Singh, N., Verhoosel, C.V., de Borst, R., van Brummelen, E.H., 2016. A fracture-controlled path-following technique for phase-field modeling of brittle fracture. Finite Elem. Anal. Des. 113, 14–29.
Spetz, A., Denzer, R., Tudisco, E., Dahlblom, O., 2021. A modified phase-field fracture model for simulation of mixed mode brittle fractures and compressive cracks in porous rock. Rock Mech. Rock Eng. 54 (10), 5375–5388.
Tian, F., Tang, X., Xu, T., Yang, J., Li, L., 2019. A hybrid adaptive finite element phase-field method for quasi-static and dynamic brittle fracture. Int. J. Numer. Methods Eng. 120 (9), 1108–1125.
Tkalich, D., Fourmeau, M., Kane, A., Li, C., Cailletaud, G., 2016. Experimental and numerical study of kuru granite under confined compression and indentation. Int. J. Rock Mech. Min. 87, 55–68.
Verma, R.K., Nguyen, G.D., Karakus, M., Taheri, A., 2024. A size-dependent energy-based strain burst criterion. Int. J. Numer. Anal. Model. 48 (12), 3186–3209.
Wang, S.S., Xu, W.Y., 2020. A coupled elastoplastic anisotropic damage model for rock materials. Int. J. Damage Mech. 29 (8), 1222–1245.
Wang, S.S., Wang, H.L., Xu, W.Y., Qian, W., 2019. Investigation on mechanical behaviour of dacite under loading and unloading conditions. Géotech. Lett. 9 (2), 130–135.
Wang, S., Zhang, J., Zhao, L., Zhang, W., 2021. Phase field modeling of anisotropic tension failure of rock-like materials. Front. Phys. 9, 809417.
Wang, S., Yang, S., Zhang, Q., Shen, W., Zhang, J., Huang, Q., 2024. A modified phase-field model simulating multiple cracks propagation of fissured rocks under compressive or compressive-shear conditions. Theor. Appl. Fract. Mech. 133, 104549.
Wang, S., Zhang, Q., Huang, Q., Yin, P., Zhang, J., 2025a. An elastoplastic damage model for stratified rocks using Pietruszczak–Mroz anisotropic theory. J. Rock mech. Geotech. 17 (10), 6234–6247.
Wang, S., Zhang, Q., Luo, H., Lin, Z., 2025b. Experimental and constitutive modeling investigations on marble in jinping underground laboratory. Deep undergr. Sci. Eng 1–14.
Wong, T.F., Baud, P., 2012. The brittle-ductile transition in porous rock: a review. J. Struct. Geol. 44, 25–53.
Wu, J.-Y., Huang, Y., Zhou, H., Nguyen, V.P., 2021. Three-dimensional phase-field modeling of mode I+ II/III failure in solids. Comput. Methods Appl. Math. 373, 113537.
Xiao, Y.-X., Feng, X.-T., Feng, G.-L., Liu, H.-J., Jiang, Q., Qiu, S.-L., 2016. Mechanism of evolution of stress–structure controlled collapse of surrounding rock in caverns: a case study from the baihetan hydropower station in China. Tunn. Undergr. Space Technol. 51, 56–67.
Yang, L., Yang, Y., Zheng, H., 2021. A phase field numerical manifold method for crack propagation in quasi-brittle materials. Eng. Fract. Mech. 241, 107427.
Yang, S.-Q., Tian, W.-L., Ranjith, P., Liu, X.-R., Chen, M., Cai, W., 2022. Three-dimensional failure behavior and cracking mechanism of rectangular solid sandstone containing a single fissure under triaxial compression. Rock Mech. Bull. 1 (1), 100008.
You, T., Zhu, Q.-Z., Li, P.-F., Shao, J.-F., 2020. Incorporation of tension-compression asymmetry into plastic damage phase-field modeling of quasi brittle geomaterials. Int. J. Plast. 124, 71–95.
Yu, Z., Shao, J.-F., Vu, M.-N., Armand, G., 2021a. Numerical study of thermo-hydro-mechanical responses of in situ heating test with phase-field model. Int. J. Rock Mech. Min. 138, 104542.
Yu, Z., Shao, J., Duveau, G., Vu, M.-N., Armand, G., 2021b. Numerical modeling of deformation and damage around underground excavation by phase-field method with hydromechanical coupling. Comput. Geotech. 138, 104369.
Yu, Z., Shao, J., Zhu, Q., 2022. Numerical Analysis of Damage by phase-field Method Handbook of Damage Mechanics: Nano to Macro Scale for Materials and Structures. Springer.
Zhang, X., Sloan, S.W., Vignes, C., Sheng, D., 2017a. A modification of the phase-field model for mixed mode crack propagation in rock-like materials. Comput. Methods Appl. Math. 322, 123–136.
Zhang, X., Vignes, C., Sloan, S.W., Sheng, D., 2017b. Numerical evaluation of the phase-field model for brittle fracture with emphasis on the length scale. Comput. Mech. 59, 737–752.
Zhang, L., Tang, S., Zhang, Y., 2024. Numerical investigation of failure mode transitions in rock specimens containing non-persistent joints under compression-shear conditions. Rock Mech. Rock Eng. 57 (10), 7905–7928.
Zhao, S., Li, P., Wang, T., Tan, Y., Fan, H., Wang, Q., 2023. A phase-field model for thermo-elastic fracture in quasicrystals. Eng. Fract. Mech., 109432
Zhou, S., Rabczuk, T., Zhuang, X., 2018. Phase field modeling of quasi-static and dynamic crack propagation: COMSOL implementation and case studies. Adv. Eng. Software 122, 31–49.
Zhou, Z., Zhao, Y., Bi, J., Zhang, Y., Wang, C., Li, Y., 2023. A thermodynamically consistent SPH-PFM model for modelling crack propagation and coalescence in rocks. Theor. Appl. Fract. Mech. 127, 104085.
Zhu, Q.Z., Shao, J.F., Kondo, D., 2011. A micromechanics-based thermodynamic formulation of isotropic damage with unilateral and friction effects. Eur. J. Mech. Solid. 30 (3), 316–325.
Zhuang, X., Li, X., Zhou, S., 2023. Transverse penny-shaped hydraulic fracture propagation in naturally-layered rocks under stress boundaries: a 3D phase field modeling. Comput. Geotech. 155, 105205.

Dr. Susheng Wang is an associate professor at Shaoxing University, China. He received his PhD in Geotechnical Engineering from Hohai University, China, in September 2020. He was funded by the China Scholarship Council to undertake a 16-month joint PhD program at the University of Lille, France. His research primarily focuses on deep rock mechanics and underground engineering. He has received honors such as the Jiangsu Province Excellent Doctoral Dissertation Award. He has hosted several research projects, including the National Natural Science Foundation of China (NSFC) Youth Fund, China Postdoctoral Science Foundation, and Open Fund of Key Laboratories, and participated in four other NSFC projects. He has published more than 30 papers indexed by SCI or EI. He is a member of the 8th Rock Mechanics Testing Committee of the Chinese Society for Rock Mechanics and Engineering, a young editorial board member of the *International Journal of Mining Science and Technology* (IJMST), and a reviewer for more than 10 scientific journals.